

Utah State University

DigitalCommons@USU

All Graduate Theses and Dissertations, Fall
2023 to Present

Graduate Studies

5-2024

Mechanical Properties and Microstructure of Multi-Materials Fabricated Through a Combination of LPBF and DED Additive Manufacturing Techniques

Christopher J. Bettencourt

Utah State University, christopher.bettencourt@usu.edu

Follow this and additional works at: <https://digitalcommons.usu.edu/etd2023>



Part of the [Mechanical Engineering Commons](#)

Recommended Citation

Bettencourt, Christopher J., "Mechanical Properties and Microstructure of Multi-Materials Fabricated Through a Combination of LPBF and DED Additive Manufacturing Techniques" (2024). *All Graduate Theses and Dissertations, Fall 2023 to Present*. 101.

<https://digitalcommons.usu.edu/etd2023/101>

This Thesis is brought to you for free and open access by the Graduate Studies at DigitalCommons@USU. It has been accepted for inclusion in All Graduate Theses and Dissertations, Fall 2023 to Present by an authorized administrator of DigitalCommons@USU. For more information, please contact digitalcommons@usu.edu.



MECHANICAL PROPERTIES AND MICROSTRUCTURE OF MULTI-MATERIALS
FABRICATED THROUGH A COMBINATION OF LPBF AND DED ADDITIVE
MANUFACTURING TECHNIQUES

by

Christopher J. Bettencourt

A thesis submitted in partial fulfillment
of the requirements for the degree

of

MASTER OF SCIENCE

in

Mechanical Engineering

Approved:

Nadia Kouraytem, Ph.D.
Major Professor

Ryan Berke, Ph.D.
Committee Member

Yanqing Su, Ph.D.
Committee Member

D. Richard Cutler, Ph.D.
Vice Provost
of Graduate Studies

UTAH STATE UNIVERSITY
Logan, Utah

2024

Copyright © Christopher J. Bettencourt 2024

All Rights Reserved

ABSTRACT

Mechanical Properties and Microstructure of Multi-Materials fabricated Through a
Combination of LPBF and DED Additive Manufacturing Techniques

by

Christopher J. Bettencourt, Master of Science

Utah State University, 2024

Major Professor: Dr. Nadia Kouraytem
Department: Mechanical and Aerospace Engineering

Mechanical and microstructural analyses were performed on multi-material samples. Before manufacturing the multi-material, three candidate materials were tested, namely, SS316L, IN625, and H282. SS316L and IN625 were selected. Joining of the two alloys was accomplished by a novel approach using two additive manufacturing techniques combined. IN625 was deposited using the additive method of DED onto the SS316L base metal that was manufactured by LPBF. Two joints were tested, namely, Direct Transition and 50/50 (intermediate zone). The direct transition samples were made by depositing 100% DED IN625 onto 100% LPBF SS316L. The 50/50 samples were made by depositing two intermediate layers of 50% SS316L and 50% IN625 powder mixed in-situ using DED between 100% IN625 and 100% SS316L. Mechanical properties of samples fabricated by both transition strategies were compared to wrought and additively manufactured single alloy samples. Both joint types exhibited significantly enhanced yield strength when compared to the additively manufactured single alloy samples. The 50/50 transition demonstrated brittle fracture. Scanning Electron Microscopy revealed microcracks at the 50/50 interface.

(68 pages)

PUBLIC ABSTRACT

Mechanical Properties and Microstructure of Multi-Materials Fabricated Through a
Combination of LPBF and DED Additive Manufacturing Techniques

Christopher J. Bettencourt

This research explores the use of different metals combined through 3D-printing to enhance the performance of materials, with a focus on making heat exchangers more cost-effective for renewable energy. The goal is to replace a costly high-temperature alloy with a more affordable low-temperature alloy, using metal additive manufacturing for its benefits such as less material waste, faster production, reduced weight, and the ability to print entire assemblies in one go. The study delves into a unique combination of two 3D-printing techniques, Directed Energy Deposition and Laser Powder-Bed Fusion, to create a multi-material composed of stainless steel 316L and a nickel-based superalloy, Inconel 625. The primary focus is on understanding the structure and properties of this material, documenting mechanical properties, and characterizing its microstructure. By investigating how these additive manufacturing techniques influence the material's structure and properties, the research provides valuable insights on the fabrication of multi-materials. It expands our understanding of how combining different 3D-printing methods can enhance the production of multi-material components.

ACKNOWLEDGMENTS

I would like to thank Dr. Nadia Kouraytem for her help and guidance throughout my degree and securing the funding for my portion of the research project funded by the U.S. Department of Energy, Office of Science, Solar Energy Technology Office, under Award Number DE-EE0009381.

I give special thanks to my wife for her encouragement and support, especially during the more difficult times. I could not have done it without her. My family, mentors, and colleagues were vital to my success, and I appreciate the time, effort, and expertise they provided.

Many thanks to my thesis committee for providing their expertise and input on this work. Thank you for making this achievement possible.

Christopher J. Bettencourt

CONTENTS

	Page
ABSTRACT	iii
PUBLIC ABSTRACT	iv
ACKNOWLEDGMENTS	v
LIST OF TABLES	viii
LIST OF FIGURES.....	ix
1 INTRODUCTION.....	1
2 OBJECTIVES	5
3 MICROSTRUCTURAL CHARACTERIZATION OF THE TRANSITION IN SS316L AND IN625 BIMETALLIC FABRICATED USING HYBRID ADDITIVE MANUFACTURING ...	6
3.1 Introduction	7
3.2 Methodology	10
3.2.1 Fabrication.....	11
3.2.2 Electron Backscatter Diffraction.....	13
3.2.3 Micro-hardness	14
3.3 Results and Discussion	14
3.3.1 Single Alloys.....	14
3.3.2 Dual Materials	16
3.4 Conclusion.....	21
3.5 Acknowledgements	23
3.6 Declarations	23
3.7 Appendix.....	24
4 BONDING SS316L AND IN625 THROUGH LASER POWDER BED FUSION AND DIRECTED ENERGY DEPOSITION: A COMPARATIVE TENSILE ANALYSIS.....	25
4.1 Introduction	26
4.2 Materials and Methods	29
4.2.1 Sample Preparation.....	30
4.3 Results and Discussion	33
4.4 Conclusion.....	43
4.5 Declaration of Competing Interest.....	45
4.6 Acknowledgements	45
4.7 Data Availability.....	45

5 DED H282 PRELIMINARY TEST.....	46
5.1 Introduction	46
5.2 Methodology	46
5.3 Results and Discussion	46
6 CONCLUSION.....	49
References	51

LIST OF TABLES

	Page
Table 3.1. Process Parameters for LPBF SS316L and DED IN625 Alloys.....	12
Table 3.2. Composition of prominent elements of Praxair SS316 powder (weight %).	12
Table 3.3 IN625 powder composition of prominent elements Praxair NI-328-17 (wt%)	13
Table 4.1 Composition of prominent elements of Praxair TruForm 316-3 Powder (wt %)	31
Table 4.2 Processing Parameters of LPBF SS316L fabricated on an Additive Industries MetalFAB1	31
Table 4.3 IN625 powder composition of prominent elements Praxair NI-328-17 (wt%)	32
Table 4.4 DED Processing Parameters (Average Value or Set Point) used on the FormAlloy L5 machine.....	32

LIST OF FIGURES

	Page
Fig. 1.1	Three types of transition strategies for combining 100% material A and 100% material B where material C is an intermediate zone..... 1
Fig. 3.1	Single alloy LPBF SS316L IPFZ maps, grain size distribution, and pole figures. The build direction is identified with an arrow on the IPF map... 15
Fig. 3.2	Single alloy DED Inconel 625 IPFZ map, grain size distribution, and pole figures. The build direction is identified with an arrow on the IPF map... 16
Fig. 3.3	Microstructural characterization of the bimetallic specimens fabricated using LPBF SS316L bases where IN625 is deposited. Two transition strategies are employed, namely a direct transition (a, c) and a 50/50 transition where an equal mix of the two powders is used over an equivalent of two DED layers (b, d). The transition zones are identified with a dashed line and further labeled on the figures. Figures (a-b) show the band contrast highlighting the grain boundaries, (c-d) show the IPF-Z maps revealing the grain orientations..... 17
Fig. 3.4	EDS maps of the Direct Transition specimen showing elemental composition and the sum spectrum weight percentages..... 19
Fig. 3.5	EDS maps of the 50/50 Transition sample showing elemental composition and the sum spectrum weight percentages..... 19
Fig. 3.6	Left: Image of the specimen fabricated by depositing IN625 DED onto the top and bottom of LPBF SS316L in a 50/50 transition (top portion) and direct transition (bottom portion). Right: Variability of the Vickers Hardness along each of the areas of interest including the single material and transition zones, and values from literature [11], [43]–[48]..... 21
Fig. 3.7	Mechanical properties from literature for both SS316L processed by LPBF and IN625 fabricated via DED. Left: Average Ultimate Tensile Strength, Middle: Average Yield Strength, Right: Average Percent Elongation [44], [49]–[52]...... 24
Fig. 3.8	Thermal conductivity values from literature for both DED IN625 (shown in red, yellow, and orange) and LPBF SS316L (shown in blue), with the exception of Halmesova et al. showing values for DED SS316L (indicated by arrow and asterisk [52]–[57])...... 24

Fig. 4.1	Comparing engineering stress-strain curves of wrought SS316L to LPBF SS316L. The image of the build plate shows an YZ orientation. The fractography image (a) shows ductile failure of LPBF SS316L and (b) shows the wrought SS316L.....	34
Fig. 4.2	Comparing engineering stress-strain curves of annealed wrought sheet coil IN625 to DED IN625 including directionality. Curves labeled a, b, and c correspond to the fractography images showing black particles.	35
Fig. 4.3	Images of EDS analysis showing magnified images and chemical composition of particle found at the fracture surfaces of some IN625 samples fabricated by powder-fed DED.....	36
Fig. 4.4	Comparing engineering stress-strain curves of joining methods, namely, direct transition and 50/50 intermediate transition in DED IN625 deposited onto LPBF SS316L. Curves labeled a and b correspond to the fractography images (a) and (b) showing striations at the fracture surfaces.	37
Fig. 4.5	Comparison of median values of the tensile properties of single-alloy samples and multi-materials.....	39
Fig. 4.6	Side-by-side comparison of post-mortem tensile dogbones a) 50/50 transition b) direct transition samples.....	40
Fig. 4.7	EDS line scans across the fracture surface of a 50/50 transition sample (left) and a direct transition sample (right) where blue represents the Fe content and orange is the Ni.....	40
Fig. 4.8	SEM montage images of microcracks at the 50/50 transition in the multi-material samples.	41
Fig. 4.9	Comparison of mechanical properties for average values from literature compared to median values of the current work. Zhang printed IN625 onto SS316L via DED with a 2 mm transition zone [11]. Ghanavati printed LPBF IN718 onto SS316L with a 4 mm transition zone [58]. Yang (DED) and Singh (LPBF) both used the print sequence of SS316L onto IN718 [18], [59].	42
Fig. 5.1	Geometry of tensile samples.	46
Fig. 5.2	Microstructural results of H282 manufactured by DED showing an IPF-Z map, a histogram of grain diameter, and inverse pole figures with x, y, and z from left to right.	47

Fig. 5.3 Stress-strain curves for H282 manufactured through DED with samples tested in three different orientations (XY, YZ, and Z), fractography images from samples that differed in response when compared to the other samples (right)..... 48

CHAPTER 1
INTRODUCTION

Multi-materials are structures made of two or more different materials [1]. Unlike conventional materials, multi-materials contain dissimilar materials at different locations within a component. These materials yield varied properties at various locations. In addition to improving multifunctionality, they reduce cost and weight of parts while providing better performance [2]. There are several methods for joining materials together. The focus of this thesis will be on Additive Manufacturing (AM) techniques. The transitions between the two materials can vary and some popular transition strategies include direct transitions, graded transitions, and intermediate layer transitions see Fig. 1.1 Three types of transition strategies for combining 100% material A and 100% material B where material C is an intermediate zone.. Direct transitions are also referred to as bimetals and graded transitions can be referred to as Functionally Graded Materials (FGMs).

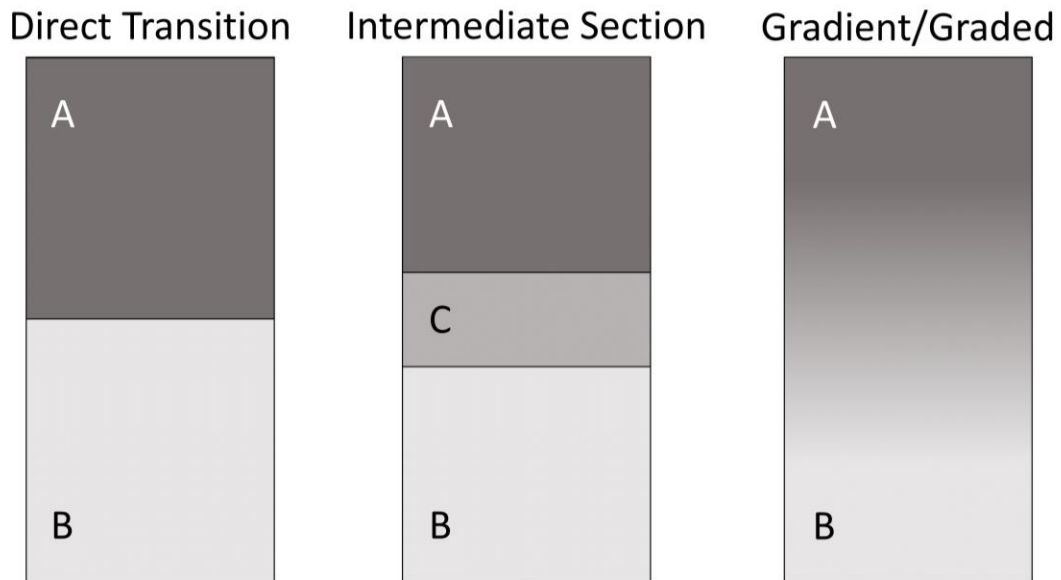


Fig. 1.1 Three types of transition strategies for combining 100% material A and 100%

material B where material C is an intermediate zone.

Research in Multi-material Additive Manufacturing (MMAM), also known as Multi-material 3D printing, has been growing. There were 5 times more publications in 2021 than in 2017 [3]. This interest stems from the benefits of AM compared to traditional manufacturing. AM is the process of fabricating a part by adding layers of material rather than traditional subtractive methods where material is cut away. MMAM offers benefits in streamlining manufacturing, enhancing design flexibility, and lowering prototype production time and costs when compared to traditional methods. This emerging field empowers 3D printed parts with customizable material properties, proving particular value in aerospace, defense, medical, and nuclear energy sectors [2].

Two additive processes are popular for multi-material manufacturing, namely Laser Powder Bed Fusion (LPBF) and Directed Energy Deposition (DED) [4]. LPBF produces parts by selectively melting geometry using a laser on a bed of powder. The bed moves down, and a new layer of powder is spread for the next layer of melting. The DED method injects powder or wire feedstock directly into a meltpool generated by an energy source. Among the materials fabricated by these techniques that are under investigation in the current thesis include stainless steel 316L (SS316L) and nickel-based superalloys such as Inconel 625 (IN625) and Haynes 282 (H282). Stainless steel and nickel-based superalloys are of interest for many harsh environment applications such as nuclear power plants, oil refineries, and aerospace engines due to their high strength, excellent toughness, and resistance to corrosion [5], [6].

LPBF technology is currently less suitable in terms of producing defect-free multi-materials compared to DED [2]. To make multi-materials with LPBF, it is necessary to modify the powder recoater to allow for multiple powders or mix the

powders together by hand in the powder reservoir. This allows for a variation in composition but is limited to vertical changes in material. For depositing different powders within the same layer, methods such as ultrasonic vibration, electrostatic, and pneumatic pressure powder deposition are necessary to modify the existing systems. The main advantage of LPBF is the high resolution relative to DED while having the disadvantage of low productivity [7].

DED has been widely used for producing multi-material components [8]. The main advantage being the availability of a wide range of materials and that material interfaces are created with high strength bonding [9]. This is due to the ability to mix various powders during the deposition process for powder-based DED [6]. However, there remain drawbacks to using the DED technique to produce multi-materials. Disadvantages include the imprecise dimensional accuracy, the presence of residual thermal stress, the need for a controlled atmosphere, cross-contamination of powders, and the necessity for post-processing [9].

The research surrounding MMAM of Stainless Steel and Inconel components is relatively new. One of the earliest efforts from 2005 studied a technique called laser rapid forming using a SS316L and a Nickel-based superalloy that was functionally graded to produce a linear change from 100% SS316L to 100% Rene88DT [10]. Since then, several articles have discussed the combination of SS316L with IN625 or similar alloys [1], [5], [11]–[18].

The objective of this research is to evaluate the mechanical and microstructural analyses of multi-material samples. Before manufacturing the multi-material, three candidate materials were tested, namely, SS316L, IN625, and H282. SS316L and IN625

were selected. Joining of the two alloys was accomplished by a novel approach combining LPBF and DED. IN625 was deposited using DED onto the SS316L base metal that was manufactured by LPBF. Two joints were tested, namely, Direct Transition and 50/50 (intermediate zone). The direct transition samples were made by depositing 100% DED IN625 onto 100% LPBF SS316L. The 50/50 samples were made by depositing two intermediate layers of 50% SS316L and 50% IN625 powder mixed in-situ using DED between 100% IN625 and 100% SS316L. Mechanical properties of samples fabricated by both transition strategies were compared to wrought and additively manufactured single alloy samples. Both joint types exhibited significantly enhanced yield strength when compared to the additively manufactured single alloy samples. The 50/50 transition demonstrated brittle fracture. Scanning Electron Microscopy revealed microcracks at the 50/50 interface.

The remainder of this document presents one publication accepted to the JOM journal in 2023 and another that is in the submission process to the journal Materials & Design. The first publication documents the microstructure of multi-material samples consisting of SS316L fabricated through LPBF and IN625 manufactured via DED. The second publication reviews the tensile properties of the multi-material samples and compares two different joining strategies, assesses failure origins, and compares results to single alloy samples and literature values. Finally, overall conclusions are drawn for all efforts undertaken during this thesis research work and both publications.

CHAPTER 2

OBJECTIVES

1. Perform preliminary Ni candidate material testing to determine which alloy to combine with SS316L. The success criterion is whether or not the tensile properties are within 10% of the minimum requirements of the ASTM standard for the wrought material. Inconel 625 and Haynes 282 are both tested.
2. Examine and document microstructure of the multi-material made from Inconel 625 manufactured by Directed Energy Deposition and Stainless Steel manufactured by Laser Powder-bed Fusion. Compare the single alloy materials to the multi-material microstructure.
3. Analyze the tensile behavior of the multi-material compared to the single alloy counterparts. Determine which joining strategy is superior.

CHAPTER 3
MICROSTRUCTURAL CHARACTERIZATION OF THE TRANSITION IN SS316L
AND IN625 BIMETALLIC FABRICATED USING HYBRID ADDITIVE
MANUFACTURING¹

Christopher J. Bettencourt and Nadia Kouraytem
Utah State University, Logan, Utah 84322-4130

Nearly all energy technologies utilize heat exchangers and recuperators within the power cycle. To further improve the cost-effectiveness of recuperators, costly high temperature Inconel 625 superalloy was substituted with a more affordable Stainless Steel 316L to be used at the low-temperature side of the heat exchanger. Bimetallic samples for analysis and examination were fabricated by combining Laser Powder-bed Fusion and Directed Energy Deposition. Two transition strategies for joining to the laser powder-bed fusion steel were explored, namely, a direct transition and an intermediate layer of 50% nickel powder mixed with 50% steel powder through Directed Energy Deposition. The microstructure and chemical composition of the multi-material structures were compared to the single alloy counterparts. Iron rich regions within the 50/50 transition zone suggest elemental segregation during the deposition of the 50/50 mixed zone. Vickers hardness values measured using micro-indentation are presented across both types of transitions and show a relative lower value in the 50/50 mixed zone.

¹ This paper was published in 2023 as:
C. J. Bettencourt and N. Kouraytem, "Microstructural Characterization of the Transition in SS316L and IN625 Bimetallic Fabricated Using Hybrid Additive Manufacturing," JOM, Oct. 2023, doi: 10.1007/s11837-023-06119-4.

3.1 Introduction

Energy consumption is projected to increase as much as 15% while the United States has the goal to reach net zero Greenhouse Gas Emissions by 2050 [19], [20]. This requires renewable energy sources to replace fossil fuel sources while simultaneously ramping production to meet ever-growing energy demand. Specifically, Concentrated Solar Power (CSP) has recently gained attention due to its potential for producing clean energy at a reasonable cost [21], [22].

One of the challenges holding back CSP from being more widely implemented is the cost of fabricating recuperators (heat exchangers). High-temperature recuperators alone account for 25-30% of the overall turbo-generator cost in a power system [23]. To enable higher cost effectiveness, substituting the high-temperature material with a low cost material has been explored. McDonald estimated a cost savings of 60% if SS347 was substituted with IN625 in a counterflow recuperator used for microturbine applications [24]. McDonald proposed the substitution of IN625 by SS347 using an automated spiral foil wrapping fabrication method.

Combining alloys is referred to as multi-material, bimetallics, or Functionally Graded Materials (FGM). FGMs have become popular over the last 20 years where yearly publications on the topic have tripled since the year 2000 [25]. Over the past decade, manufacturing FGMs has been shifting from traditional methods such as, vapor deposition, thermal spray, and powder metallurgy, to Additive Manufacturing (AM) due to the design freedom, reduced manufacturing steps, lower cost, and better production cycles [2], [26], [27].

AM is a suite of manufacturing processes in which materials are fabricated in a layer-by-layer method to yield a three-dimensional part. Of interest to metal fabrication, Laser Powder Bed Fusion (LPBF) is a common process of AM in which the metal powder is swept onto the build plate one layer at a time then particles are selectively fused using a high-powered laser, the build plate is lowered and the cycle is repeated. Directed Energy Deposition (DED) on the other hand is an AM process that is gaining popularity especially in large scale manufacturing and repair. DED deposits powder or wire feedstock concentrically with a high powered laser which simultaneously melts the material as it is deposited. DED results in lower resolution parts and larger feature capabilities when compared to LPBF. DED machines are sometimes equipped with several hoppers that enable depositing of multi-materials, in contrast, LPBF requires changing powder feedstock or making expensive upgrades to equipment to make multi-material fabrication possible.

To help enable future multi-material heat exchangers to be manufactured by AM technologies, more knowledge must be disseminated about its potential for increasing affordability. Recuperators are being built by AM to enable compact design, consolidation of component assemblies, and ability to manufacture multi-material components [28]–[30]. Six other case studies are reviewed by Kaur and Singh [31]. Very few multi-material heat exchangers have been fabricated by AM techniques [32], [33].

Two widely used metallic alloys are Stainless Steel 316L (SS316L) and Inconel 625 (IN625). SS316L provides high performance in mechanical properties and increased corrosion resistance at a low cost when compared to other similar materials [34]. IN625 on the other hand is a high-temperature alloy that is nonmagnetic, corrosion and

oxidation-resistant, and is used for its high strength and toughness [35]. The combination of these alloys can provide material cost savings when compared to using IN625 as a single material.

The joining of the two dissimilar metals has been covered in detail from various research groups. Zhang et al. tested the properties of graded IN625 with SS316L compared to single alloy counterparts processed by DED [11]. The results showed sharp microstructural variations for the direct transition sample and gradual variations for the graded layer samples. The yield strength of the graded samples approached that of pure IN625 and ultimate strength was similar to pure SS316L. Su et al. demonstrated the effect of different mixing ratios throughout the gradation of Laser Metal Deposited SS316L and IN718 multi-material [5]. The conclusion was a transition of 10% composition change every 10 layers for the intermediate layers between alloys provided the highest tensile properties and elongation, while decreasing the intermediate zone mixing to 5% produced thermal cracking. Hinojos et al. deposited IN718 onto a SS316L substrate and SS316L onto a IN718 substrate using powder-bed Electron Beam Melting [13]. Joints were characterized and it was concluded that the electron beam melting method was superior at producing a bimetallic than traditionally welded joints. Chen et al. studied the effect of build parameters on properties during deposition of IN718 tracks joined onto a SS316H substrate through LPBF [14]. The authors concluded that chemical inhomogeneity may benefit the mechanical properties by providing interlocking between the two materials. Singh et al. produced a SS316L and IN718 bimetallic with an intermediate layer between the pure alloys using LPBF and found a parameter set that produced defect free bimetallics [18]. The tensile strength approached that of SS316L. The microstructure

showed columnar grains and equiaxed grains within the transition region. Shah et al. performed a parametric study of SS316L with IN718 manufactured via DED [17]. Phases were identified, tensile, wear, and hardness properties measured while exploring the effect of varying the laser power parameter. The authors concluded that the processing parameters of DED (i.e., laser power and powder mass flow rate) were inversely proportional to the tensile strength of the functional part.

The objective of this research is the investigation of the microstructure and micro-hardness of a combination of LPBF SS316L and DED IN625 to manufacture a bimetallic. This combination of techniques can leverage the advantages of each AM technique (small features in LPBF and fast deposition in DED) and can be used as a reference for the repair of a LPBF part by DED using a dissimilar metal. In this research, a direct transition specimen and a 50/50 transition specimen were assessed to enable future research and application of bimetallic and functionally graded heat exchangers.

3.2 Methodology

In this investigation, single and bimaterial samples were manufactured using AM processes for examination of the microstructures. The SS316L and IN625 materials were manufactured using LPBF and DED, respectively, and the pure single alloys were examined as reference materials. Bimaterial samples were manufactured by depositing DED IN625 onto LPBF SS316L. Two transition strategies were investigated, namely a direct transition in which no mixing of powders occurred and a 50/50 mixing strategy in which the two alloy powders were mixed during the DED process for two layers 600 μm before the transition to pure DED IN625. See below for critical characteristics of both alloys from literature values.

3.2.1 Fabrication

3.2.1.1 Laser Powder Bed Fusion

The SS316L powder used was made by gas atomization by Praxair. The Additive Industries MetalFAB1 was used to produce the SS316L single alloy as well as the SS316L section of the bi-metallic specimens. Argon was used as inert gas in the build chamber. The system was equipped with four SPI Red Power (500-Watt, 1,070 wavelength) lasers with full field coverage that allow it to produce several parts at once or work on larger parts with all four lasers capable of scanning a single part simultaneously. A layer thickness of 50 μm and a chess scanning strategy was used. Recommended optimal processing parameters were used by Addman Engineering to fabricate the SS316L and are detailed in Table 3.1. The LPBF parts were stress-relieved through a ramp up to 450°C and held at that temperature for 4 hours, then furnace cooled to 200°C and air cooled to room temperature and removed from the substrate through wire electrical-discharge machining. For the elemental composition of the SS316L powders, see Table 3.2.

Table 3.1. Process Parameters for LPBF SS316L and DED IN625 Alloys

LPBF SS316L						
Hatch	Hatch	Hatch	Contour	Contour		
Spacing (μm)	Speed	Power	Speed	Power		
	(mm/s)	(W)	(mm/s)	(W)		
100	850	220	850	100		
DED IN625						
Power	Feed Rate	Flow	Spot	Shield	Carrier	Hatch Space
	(mm/min)	Rate	Dia.	Gas	Gas	Overlap (%)
		(g/min)	(mm)	(l/min)	(l/min)	
MPSC ²	Contour: 600 Infill: 800	18.75	2.5	14	7	35

Table 3.2. Composition of prominent elements of Praxair SS316 powder (weight %)

Fe	Cr	Ni	Mo	Si	Mn
Balance	16.87	12.16	2.39	0.5	0.46

3.2.1.2 Directed Energy Deposition

During DED, metal powder is deposited onto the build via a blown gas coaxial with a high-powered laser that melts the newly deposited powder onto the previously deposited layers. IN625 was deposited directly onto the LPBF SS316L specimen for the direct transition. A two-layer intermediate mixture (300 μm each, hence a total of 600

² Melt Pool Size Control (MPSC) is the in-situ closed-loop feedback cycle used by Formally to change laser power based on the size of the melt pool detected by a camera.

μm) of 50% SS316L with 50% IN625, was deposited onto the LPBF SS316L for the 50/50 transition before deposition of the 100% IN625 alloy. The powders were blended during deposition from their respective hoppers. The IN625 powder was manufactured by Praxair Surface Technologies via vacuum induction argon gas atomization. The apparent density per ASTM B212 was 4.16 g/cm^3 . The elemental composition is shown in Table 3.3. The FormAlloy L5 machine was used to fabricate the IN625. Argon gas was used as a shielding and carrier gas. The machines were equipped with a 1-kW fiber laser.

Table 3.3. IN625 powder composition of prominent elements Praxair NI-328-17 (wt%)

Ni	Cr	Mo	Fe	Nb	Co
Balance	21.38	9.09	4.00	3.72	0.10

FormAlloy employs in situ build data monitoring for analysis and real-time closed-loop control. The build parameters for the IN625 are shown in Table 3.1 and are set point values that may have varied over the build to control melt pool geometry. The test coupons were machined to thickness before experimentation.

3.2.2 Electron Backscatter Diffraction

Scanning electron microscopy (SEM) imaging was captured for the single material and transition zones of the bimetallic specimens. Samples were ground and polished on a Buehler grinder-polisher machine, vibratory polished, and cleaned with an ultrasonic bath for several hours. Images were captured using an FEI Quanta FEG 650 SEM equipped with electron backscatter diffraction (EBSD) capabilities using a NordlysMax Detector and energy dispersive spectroscopy (EDS) capabilities using an Oxford X-Max Detector. The accelerating voltage was 30 kV, with a spot size of $4.5 \mu\text{m}$, and a dwell time of $40 \mu\text{s}$. For the EBSD analysis, the step size was $3 \mu\text{m}$ with forward

scatter enabled. AZtec software was used to post-process the EBSD data and generate the inverse pole figure (IPF) maps, grain texture pole figures, and grain size distribution data. For the calculation of the average grain size, the maximum Feret diameter was used as a measure.

3.2.3 Micro-hardness

The Vickers microhardness property of the single and bimetals was tested using a witness sample with both transitions implemented into one part and tested at FormAlloy. The sample was fabricated by depositing DED IN625 onto a LPBF SS316L block using a direct transition on the bottom of the SS316L block and a 50/50 transition in which 50% of SS316L powder was mixed with 50% IN625 powder then deposited on the top of the SS316L block. The surface was polished and tested using an ALPHA-MHT-1000Z microhardness tester produced by Pace Technologies. Three repetitions for each single material and transition zone were performed and averaged. More information about the part geometry and results are presented in Sect. below.

3.3 Results and Discussion

3.3.1 Single Alloys

The IPF map, grain size distribution, and pole figures of the LPBF SS316L are shown in Fig. 1. The sample exhibits a relatively fine microstructure with grains that align with the build direction in the LPBF process see Fig. 3.1. The average grain diameter measured using maximum Feret diameter is $35.6 \mu\text{m}$, and the standard deviation is $20.7 \mu\text{m}$ with the median being $28.5 \mu\text{m}$. The distribution of grain diameters illustrates the high frequency of smaller-sized grains demonstrating a right skew of larger grains with a maximum of $177 \mu\text{m}$. The average area of the grains is $360 \mu\text{m}^2$ with an average aspect ratio of 2.28. The maximum misorientation angle is 20° . High concentration of

crystallographic orientation in the inverse pole figure is observed in the [101] crystallographic direction for the Y inverse pole figure. These results are in agreement with the general trend of grain orientations in LPBF SS316L [36]–[38].

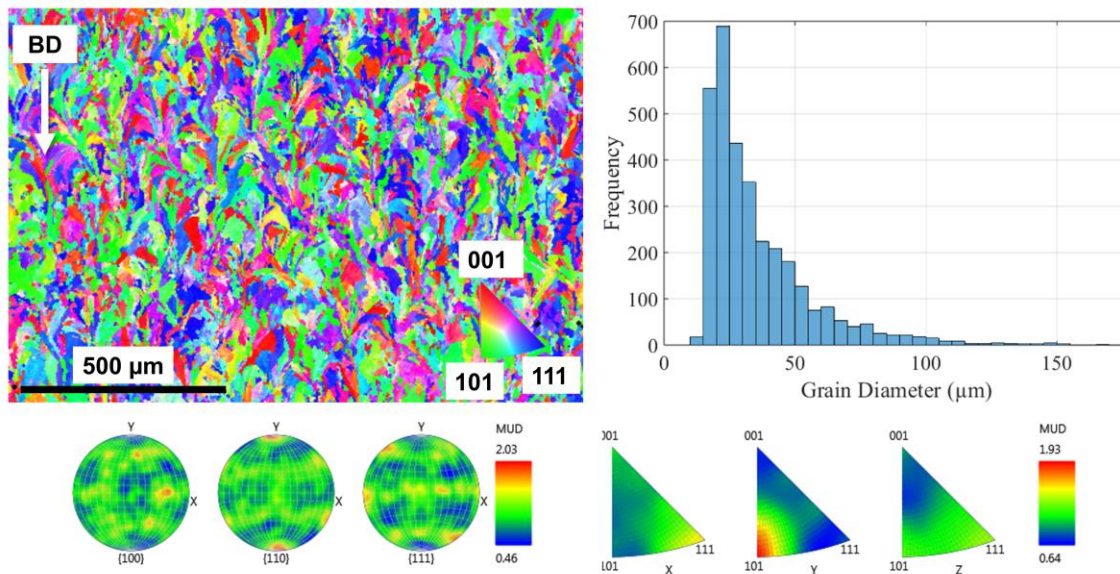


Fig. 3.1 Single alloy LPBF SS316L IPFZ maps, grain size distribution, and pole figures. The build direction is identified with an arrow on the IPF map.

The DED IN625, on the other hand, exhibits larger grains when compared with SS316L, as shown in Fig. 3.2 (note that both EBSD IPF maps were captured at the same resolution for ease of interpretation). The average grain diameter in DED IN625 is of 80.24 μm with a standard deviation of 86.96 μm and a median of 48.8 μm . The texture is shown in the inverse pole figures of Fig. 3.2. The grains are textured again in the [101] crystallographic direction of the Y inverse pole figure as well as in the [111] crystallographic direction in the X IPF texture map, which correspond to the build direction. These results are also in agreement with the general trend of the anisotropy in AM Nickel-based alloys [39]–[42].

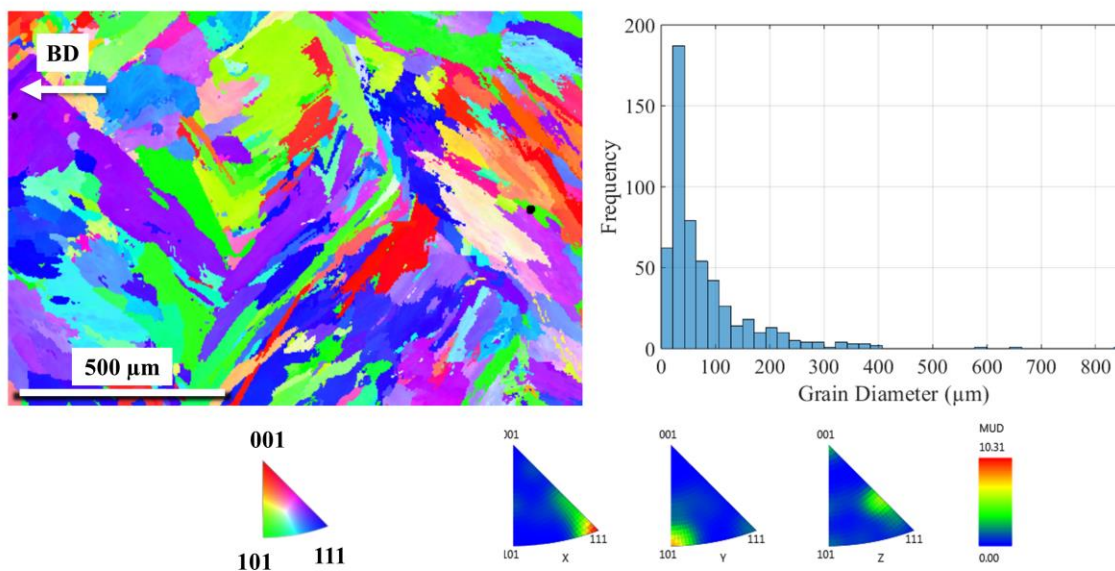


Fig. 3.2 Single alloy DED Inconel 625 IPFZ map, grain size distribution, and pole figures. The build direction is identified with an arrow on the IPF map.

3.3.2 Dual Materials

The microstructural characterization for the two transition strategies of the dual materials are compared side by side in Fig. 3.3. The band contrast BSE and IPF maps are compared side by side for the direct transition on the left and the 50/50 transition on the right. The transition zones in each transition strategy are identified using dashed lines on the band contrast images and further labeled. The band contrast images reveal an observable increase in porosity in the 50/50 layer when compared to the direct transition sample.

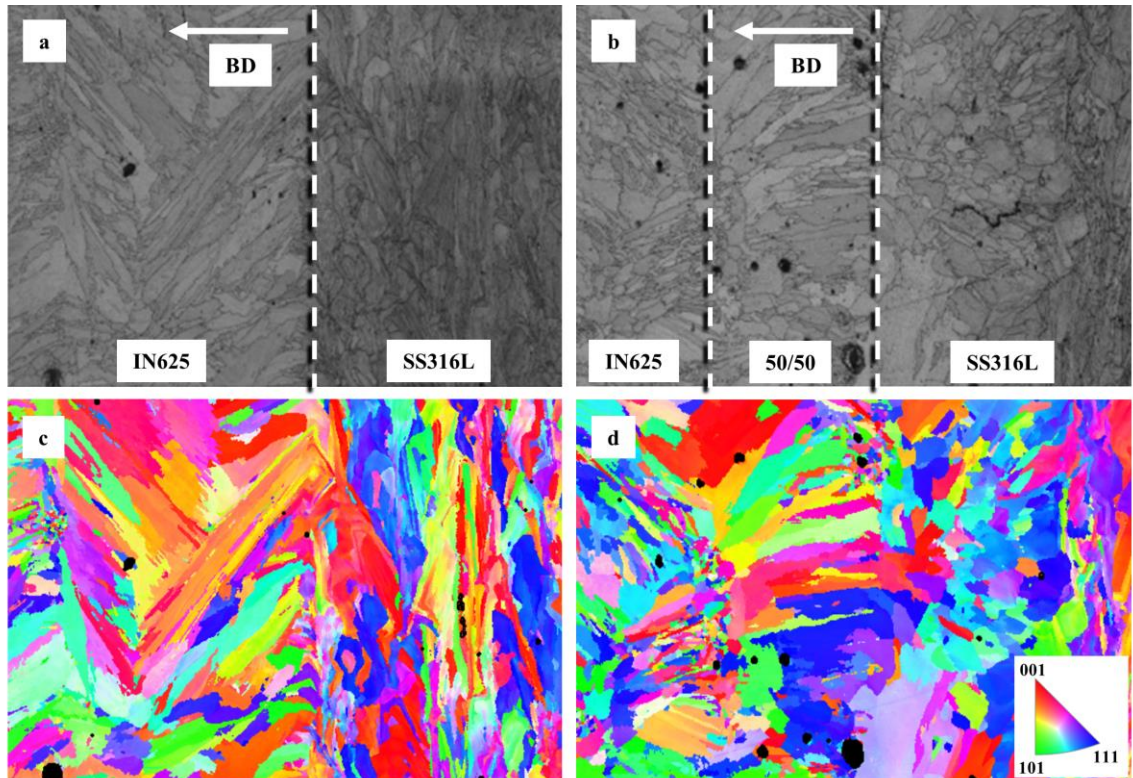


Fig. 3.3 Microstructural characterization of the bimetallic specimens fabricated using LPBF SS316L bases where IN625 is deposited. Two transition strategies are employed, namely a direct transition (a, c) and a 50/50 transition where an equal mix of the two powders is used over an equivalent of two DED layers (b, d). The transition zones are identified with a dashed line and further labeled on the figures. Figures (a-b) show the band contrast highlighting the grain boundaries, (c-d) show the IPF-Z maps revealing the grain orientations.

Comparing the IPF maps of the two samples in Fig. 3.3 (c) and (d), in the direct transition sample, the stainless steel grains exhibit limited growth, without extending into the neighboring IN625 layers. This restriction can be attributed to the sudden change in material composition, leading to a lack of favorable conditions for the continued growth of the stainless steel grains. As a result, the stainless steel grains in the direct transition sample remain confined within their original boundaries. Conversely, in the 50/50 intermediate layers of the blended transition sample, the stainless steel grains demonstrate the ability to continue their growth. The stainless steel grains successfully extend their

boundaries into the blended region. This phenomenon can be attributed to the gradual change in composition, allowing for an interfacial continuity that promotes grain growth. Overall, this comparison highlights the contrasting growth behaviors of stainless steel grains in the direct transition sample and the 50/50 SS316L-IN625 blend. While the direct transition restricts the growth of stainless steel grains, the blended sample enables their expansion into the intermediate layers, demonstrating the importance of material compatibility in facilitating grain growth with less discontinuities.

Qualitatively, the grain morphology in the SS316L side of the 50/50 appears to be more equiaxed near the transition while the direct transition sample has SS316L grains that are more columnar. This is likely due to differences in the DED processing parameters or due to the addition of 50% SS316L in the intermediate layer of the 50/50 sample causing thermal properties to differ, and leading to columnar solidification.

Another noteworthy observation at the transition zone is pertaining to the distribution of elements in the final part. Fig. 3.4 represents the EDS results for the detected elements. Examining the interface in the Fe map, a low amount of Fe is seen to diffuse into the IN625 zone. Fig. 3.5 shows the EDS maps for the 50/50 sample where a larger area that spans the 50/50 blended zone (about 600 μm wide region) exhibits an Fe-rich area that is expected from the mixing of the SS316L powders and the IN625 powders during DED. Moreover, Fe-rich pocket-like zones are clearly identified near the transition line in Fig. 3.5. It is postulated that the Fe-rich pockets are a result of elemental segregation during the deposition and solidification processes.

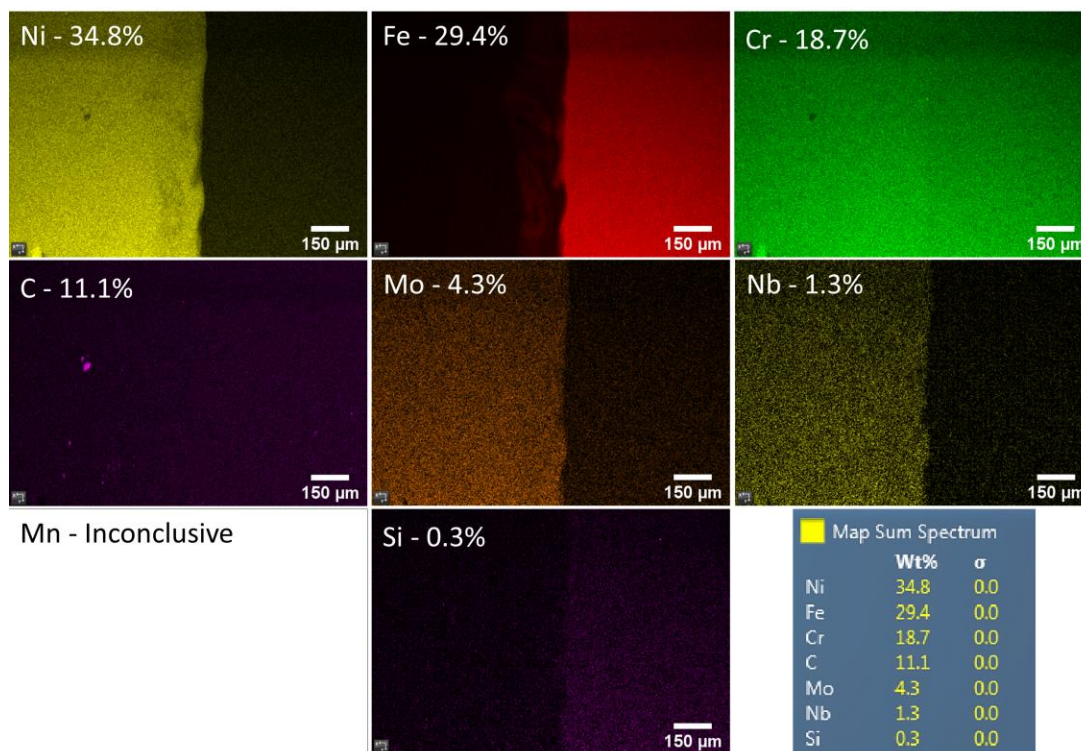


Fig. 3.4. EDS maps of the Direct Transition specimen showing elemental composition and the sum spectrum weight percentages.

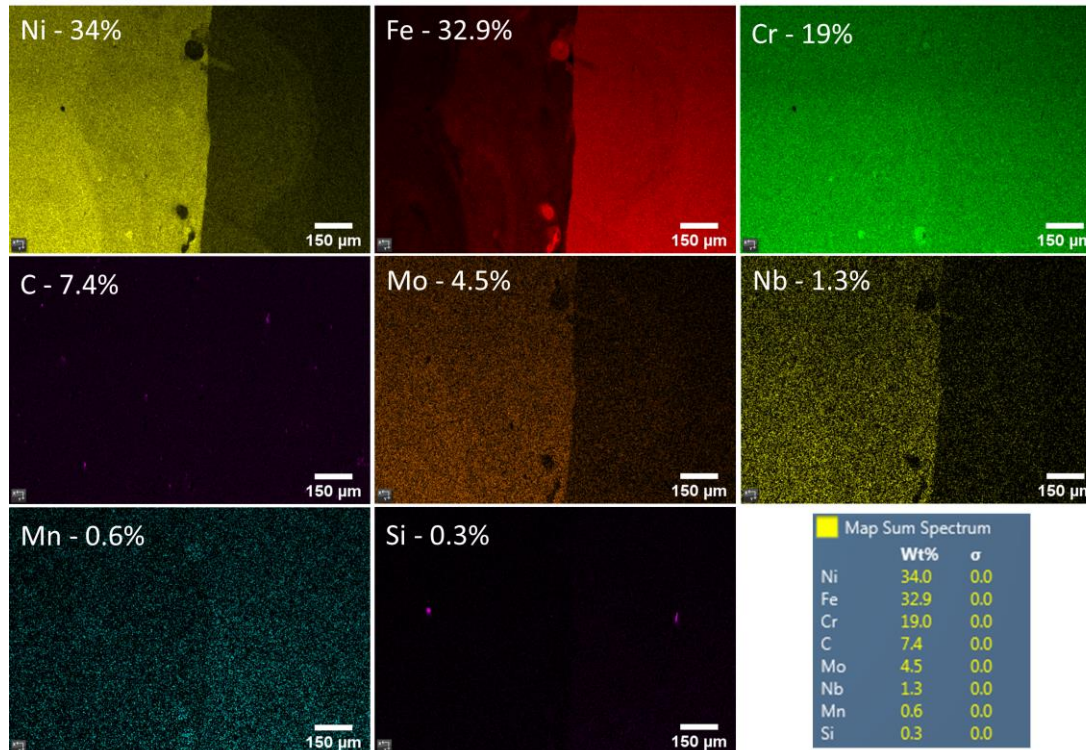


Fig. 3.5. EDS maps of the 50/50 Transition sample showing elemental composition and the sum spectrum weight percentages.

To further understand the behavior of the bimetals, the micro-hardness of both transition strategies of the bimetallic specimens are measured and shown in Fig. 3.6. For that purpose, a separate analysis specimen was fabricated by depositing IN625 on one end of a LPBF SS316L part in the direct transition and then depositing a 50/50 transition on the other end of the LPBF SS316L part. The micro-hardness of each single material and transition zone were tested. The pure IN625 exhibits HV values ranging between 241.5 and 277.1. The pure SS316L exhibits HV values ranging between 230.6 and 262.9. The direct transition strategy exhibits an average of 262.3 HV and the 50/50 transition a much lower average value of 232 HV. The authors hypothesize this is due to larger grains in the 50/50 region, or solid solution softening. It is observed that while the 50/50 transition was lower in hardness than both single alloys, the Direct Transition had increased hardness comparable with the upper value in IN625. Therefore, it is recommended that for increased hardness when producing a bimetallic to use a direct transition rather than 50/50 when DED is used to deposit IN625 onto LPBF SS316L, or a thorough investigation into optimal properties of printing a 50/50 transition layer.

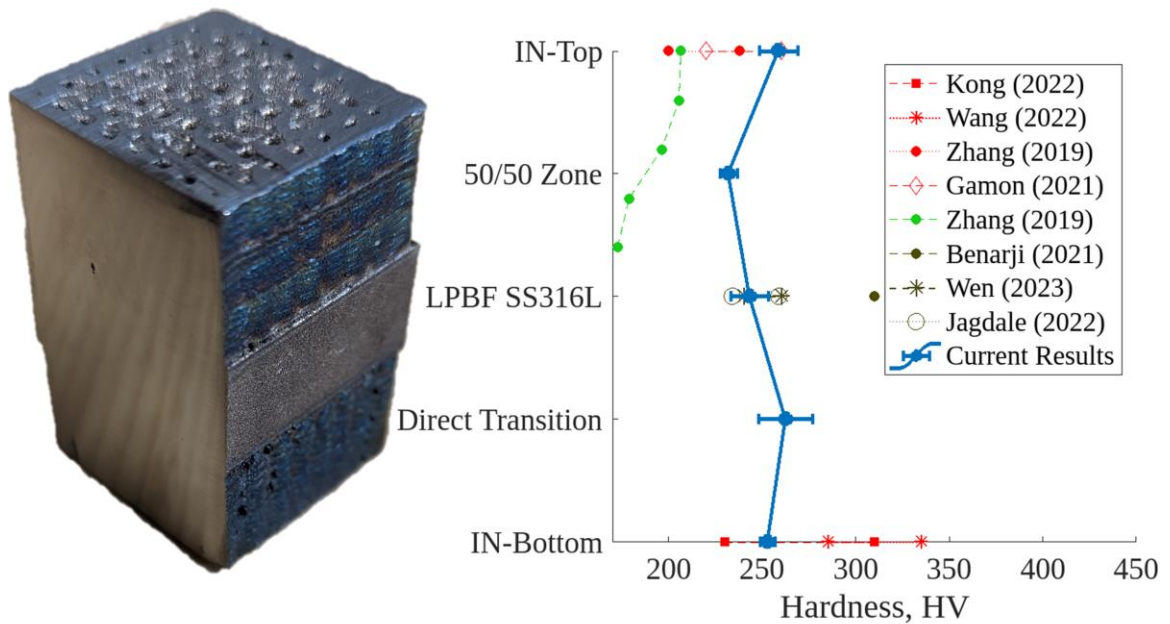


Fig. 3.6 Left: Image of the specimen fabricated by depositing IN625 DED onto the top and bottom of LPBF SS316L in a 50/50 transition (top portion) and direct transition (bottom portion). Right: Variability of the Vickers Hardness along each of the areas of interest including the single material and transition zones, and values from literature [11], [43]–[48].

3.4 Conclusion

The microstructures of single alloy LPBF SS316L and DED IN625 were analyzed along with the combinatory alloys fabricated with a direct transition and a 50/50 mixed intermediate region. The 50/50 transition zone showed an increase in porosity when compared to the direct transition. Iron-rich zones in the 50/50 section imply elemental segregation during deposition and solidification of the DED mixed layers. Microhardness showed an increased hardness at the direct transition compared to the 50/50 transition. It is therefore recommended to ensure optimal properties are determined for a 50/50 transition when joining IN625 with LPBF SS316L using DED.

Future work directions to support the energy sector in adopting AM processes include a more comprehensive study on the development of parameters to fabricate the joint of the bimetallic samples. More EBSD scans would increase the sample size and

validate trends shown in this work. Furthermore, the quality of the two transition strategies should be further investigated.

Finally, by understanding the microstructure of the direct and 50/50 transition, industry and academia can design accordingly to make use of bimetallics fabricated by DED combined with LPBF to achieve cost savings and a reduced envelope for heat exchangers in the energy sector.

3.5 Acknowledgements

This material is based upon work supported by the U.S. Department of Energy, Office of Science, Office of Energy and Renewable Energy, Solar Energy Technologies Office (SETO) under Award Number DE-EE0009381. The authors acknowledge startup funding from Utah State University. The authors are grateful for the support from the Microscopy Core Facility at Utah State University for SEM characterization, and Formalloy for micro-hardness testing.

3.6 Declarations

On behalf of all authors, the corresponding author states that there is no conflict of interest.

3.7 Appendix

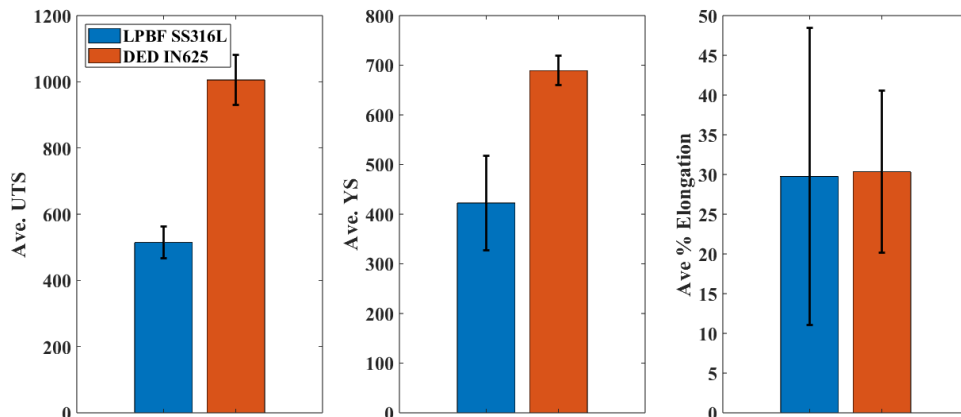


Fig. 3.7. Mechanical properties from literature for both SS316L processed by LPBF and IN625 fabricated via DED. Left: Average Ultimate Tensile Strength, Middle: Average Yield Strength, Right: Average Percent Elongation [44], [49]–[52].

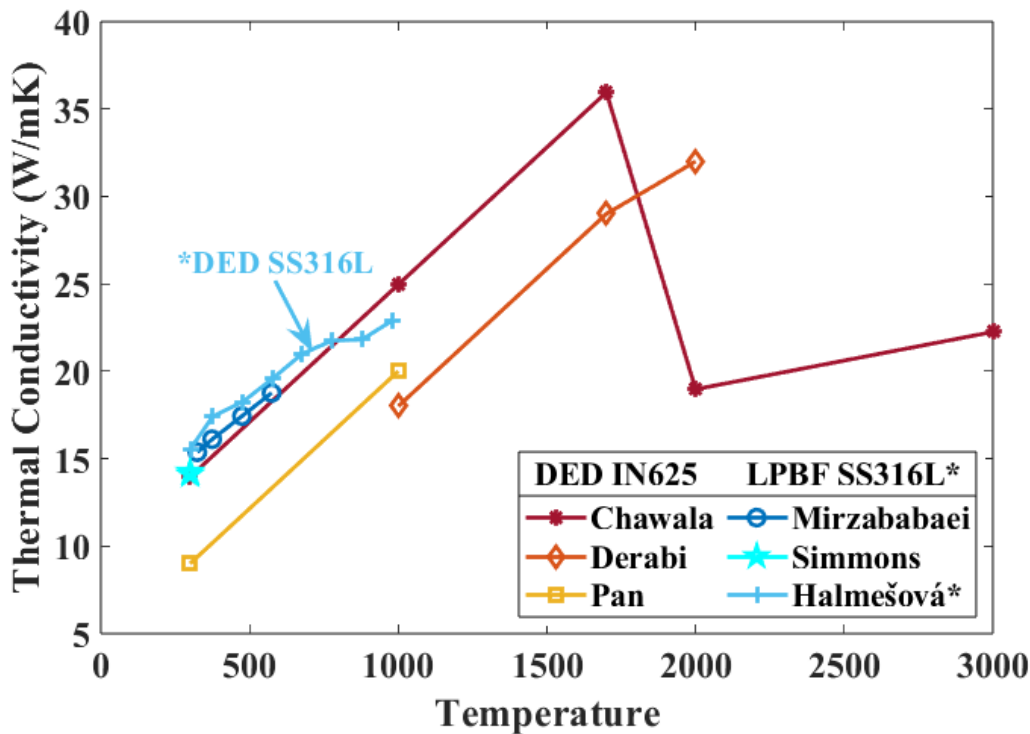


Fig. 3.8. Thermal conductivity values from literature for both DED IN625 (shown in red, yellow, and orange) and LPBF SS316L (shown in blue), with the exception of Halmesova et al. showing values for DED SS316L (indicated by arrow and asterisk [52]–[57]).

CHAPTER 4

BONDING SS316L AND IN625 THROUGH LASER POWDER BED FUSION AND
DIRECTED ENERGY DEPOSITION: A COMPARATIVE TENSILE ANALYSIS³

Christopher J. Bettencourt and Nadia Kouraytem
Utah State University, Logan, Utah 84322-4130

Directed Energy Deposition was used to deposit IN625 onto SS316L manufactured by Laser Powder Bed Fusion. The tensile properties of the resulting multi-material specimens were compared to those of the individual alloys. Two bonding joint methods were examined: a direct transition and a 50/50 intermediate layer that involved blending 50% of each alloy powder during the DED process. The study found that the combined multi-material exhibited higher yield strength than the single alloys. Further analysis revealed that the direct transition joint outperformed the 50/50 transition joint due to brittle failure observed in the 50/50 transition samples at the joint interface. Energy Dispersive Spectroscopy identified Aluminum Oxide particles that were observed in the DED-IN625 single alloy samples. Through Scanning Electron Microscopy, microcracks were observed at the interface of the 50/50 intermediate transition sample. These findings provide valuable insights into optimizing multi-material bonding techniques for applications requiring enhanced mechanical properties and highlight the importance of careful selection and design of bonding methods to ensure the desired structural integrity and performance.

³ Preprint submitted to Materials & Design in 2023

4.1 Introduction

Additive manufacturing (AM) has been an increasingly popular method for producing multi-materials [25]. Parts can have optimized mechanical properties for their intended applications which is especially useful in harsh environments of high temperature and high load and give the designer flexibility to tailor the materials to their environment [2], [4].

One method for repairing parts is an additive technique known as Directed Energy Deposition (DED). This technique is also known as laser metal deposition, direct laser deposition, or laser engineered net shaping [2]. DED is advantageous in relation to other techniques due to the size of components that can be manufactured, the in-situ multi-powder deposition capability, availability of a wide range of materials, and the ability to bond materials with high strength interfaces. The disadvantages of this process include the low dimensional accuracy of the printed parts, residual thermal stress, requirement of atmospheric control and machining processes which are necessary for quality surface finish [9].

Another well-known AM process is laser powder-bed fusion (LPBF). This method can produce high-precision small and medium-sized multi-metal parts, but with limitations on the location and orientation where different materials can be added due to the powder distribution system [2]. For multi-material manufacturing, the powders must be premixed in the hopper or the system must be upgraded to include in-layer material changes. This makes LPBF less ideal for printing with multi-materials, or at least more expensive, when compared with DED.

Several research groups have examined multi-material parts made by either of the previously mentioned AM techniques, but less so a combination of the two. Many properties are of interest when testing the bonding of two alloys together. One of the more popular properties is tensile values. These provide valuable insights into the bond strength of a multi-material. Ghanavati et al. [58] fabricated 4 types of samples using LPBF: A bimetal sample where it directly transitioned from Stainless Steel 316L (SS316L) to Inconel 718 (IN718), a 50/50 intermediate transition between the two single alloys (one that used SS process parameters and another that used IN parameters), finally a sample with a graded step composition of 25 wt%. This latter sample had the highest yield strength (YS), but the lowest elongation and broke prematurely at just 10% elongation (% El) compared to the other samples which fractured at elongations between 30 and 35%.

Zhang et al. [11] fabricated IN625 onto SS316L with intermediate layers of 50% SS and 50% IN for 2 mm via DED with pre-mixed powders. Tensile results were compared to the single alloy counterparts. The (Ultimate Tensile Strength) UTS of the multi-material was slightly higher than SS316L fabricated by DED at a value of 606 MPa. The YS approached that of single alloy DED IN625 at 406 MPa. The % El was not recorded.

Chen et al. [16] manufactured two types of multi-material samples through DED where the first type was IN625 onto SS316L and the second type was SS onto IN. They found that IN on SS exhibited less cracks and had no compositional sudden-change zone in contrast to the samples where SS was deposited onto IN. No tensile results were provided to compare to other literature values.

Yang et al. [59] studied three samples of SS316L deposited onto IN718 through DED. The first sample was non-graded (a direct transition from SS to IN), the second was graded with 25 wt% change, and the third was a graded sample with 10 wt% change. Cracks were observed in both graded samples and were attributed to differences in cooling rate and differences in coefficients of thermal expansion of the two materials. Cracks were observed in the non-graded sample at the interface between the two materials and silicon oxide inclusions were revealed and analyzed near the crack surfaces. Tensile results showed slightly higher performance for the 25 wt% graded sample when compared to the 10 wt% graded and non-graded samples. None of the multi-materials achieved tensile values above that of single alloy SS316L and did not elongate beyond 10% with the direct transition elongating 9%.

Singh et al. [18] analyzed a bimetallic (Direct Transition) composed of SS316L that transitioned directly to IN718 through LPBF. The tensile results showed that the bimetallic structure exhibited a higher UTS than that of single alloy SS316L. The elongation at break was 21% which was slightly higher than LPBF-built IN718.

Shah et al. [17] produced a thin wall structure through a type of DED process composed of IN718 deposited onto SS316L where the transition gradually changed in composition every 3 layers by 25% IN718. Tensile results revealed that the ultimate tensile strength decreased with laser power and increased with powder mass flow rate. High powder flow rate resulted in UTS between 531 and 596 MPa.

This article aims to document the tensile properties of a multi-material produced through both LPBF and DED, specifically, LPBF SS316L combined with powder-fed DED IN625. Two joining interfaces are tested, namely, direct transition and 50/50

intermediate transition (where 50% SS316L powder is blended with 50% IN625 during the DED process). The novel combination of LPBF and DED could help with several applications. In a scenario where a LPBF part has failed and needs repair, DED can be used to not only restore the part, but enable higher strength through a multi-material. Another application could be when a multi-material part is needed and might only require high resolution features at one section, but less precision at another. As AM technology continues to become more popular, LPBF combined with DED will likely be encountered to leverage the advantages of both methods. Documenting the bonding of SS316L and IN625 is paramount to enable evidence for quick decision-making in the applications mentioned above, or in other scenarios not yet explored.

4.2 Materials and Methods

Uniaxial tensile testing was performed on an MTS Bionix 370 tabletop load frame. The test was quasi-static and displacement controlled using a rate of 1 mm/min. In total, 6 groups of samples were tested: wrought samples (SS316L and IN625), AM single alloy samples (LPBF SS316L and DED IN625), and finally the two types of multi-materials (direct transition and an intermediate zone transition).

Post-processing of the tensile data was performed using MATLAB. Strain was calculated by dividing the crosshead displacement by the gauge length of 25.4 mm. The yield strength was calculated using a linear fit of data between an upper and lower limit selected by the user from the elastic portion of the stress strain curve. The 0.2% rule was used where the fit was offset to find the intersection with the stress strain curve.

For Scanning Electron Microscopy (SEM), an FEI Quanta FEG 650 scanning electron microscope was used. It was equipped with an Oxford X-Max detector for

Energy Dispersive Spectroscopy (EDS) capability. EDS and post-processing were accomplished via AZtec software. The accelerating voltage was 15 kV with a spot size of 2 μm and a dwell time of 15 μs in an approach similar to that used by the authors in [60].

4.2.1 Sample Preparation

Three types of samples were made following ASTM E8 subsize specimen standards for tensile testing: (1) wrought samples, (2) AM single alloy samples, and (3) multi-material samples. The preparation of each will be detailed.

4.2.1.1 Wrought Samples

The wrought samples were extracted from bulk material using a waterjet. The SS316L samples were extracted from SS316L 11 gauge cold rolled coil. It was solution annealed at 1040°C then air and water quenched. The average cross-sectional area was 19.64 mm^2 with a standard deviation of 0.31 mm^2 and values ranging between 19.35 mm^2 and 20.04 mm^2 . The IN625 samples were extracted from sheet made by EAF-AOD-electroslag remelted IN625 coil that was pickled and annealed. The average cross-sectional area was 20.40 mm^2 with a standard deviation of 0.24 mm^2 , a minimum value of 20.13 mm^2 , and a maximum value of 20.62 mm^2 .

4.2.1.2 AM Single Alloy Samples

The AM samples were produced through LPBF and DED. The SS316L was produced using gas-atomized Praxair TruForm316-3 powder on an Additive Industries MetalFAB1. See Table 4.1 Table 3.1 for the chemical composition of the powder and Table 4.2 for the processing parameters. The system uses four SPI Red Power (500-Watt, 1,070 nm wavelength) lasers. The samples were stress relieved at 450°C for 4 hours, furnace cooled to 200°C then air cooled. Wire Electrical Discharge Machining (EDM) was used to detach the rectangular bars from the build plate as oriented in Fig. 4.1. The

samples were then machined to size. They had an average area of 19.63 mm² with a standard deviation of 0.14 mm², a minimum value of 19.41 mm², and a maximum value of 19.75 mm².

Table 4.1. Composition of prominent elements of Praxair TruForm 316-3 Powder (wt %)

Fe	Cr	Ni	Mo	Si	Mn
Balance	16.87	12.16	2.39	0.5	0.46

Table 4.2. Processing Parameters of LPBF SS316L fabricated on an Additive Industries MetalFAB1

LPBF SS316L				
Hatch	Hatch	Hatch	Contour	Contour
Spacing	Speed	Power	Speed	Power
(μm)	(mm/s)	(W)	(mm/s)	(W)
100	850	220	850	100

The single alloy IN625 was fabricated using powder-fed DED with gas atomized Praxair Ni-328-17 powder. Chemical composition can be seen in Table 4.3. The DED system used was a FormAlloy L5 machine equipped with a 1 kW fiber laser. A proprietary software was used to maintain the optimal meltpool geometry by varying parameters with a closed-loop feedback control. Set points are seen in Table 4.4. A block sample in an L shape was printed and cut off the build plate with wire EDM. Using a waterjet, samples were extracted from the block in three orientations. The XY orientation refers to the sample having the build direction in the same direction as the thickness of the sample. The YZ orientation refers to the samples extracted with the build direction in

the same direction of the width of the sample. Finally, the Z orientation was when samples were extracted having the length of the specimen in the same direction as the build direction. This can be seen in the images overlaid onto the stress strain graphs see Fig. 4.1. The average cross-sectional area was 21.33 mm² with a standard deviation of 0.59 mm², a minimum value of 20.53 mm², and a maximum value of 22.61 mm².

Table 4.3. IN625 powder composition of prominent elements Praxair NI-328-17 (wt%)

Ni	Cr	Mo	Fe	Nb	Co
Balance	21.38	9.09	4.00	3.72	0.10

Table 4.4. DED Processing Parameters (Average Value or Set Point) used on the FormAlloy L5 machine

DED IN625						
Power	Feed Rate	Flow	Spot	Shield	Carrier	Hatch Space
	(mm/min)	Rate	Dia.	Gas	Gas	Overlap (%)
		(g/min)	(mm)	(l/min)	(l/min)	
MPSC ⁴	Contour: 600	18.75	2.5	14	7	35
	Infill: 800					

4.2.1.3 LPBF-SS316L/DED-IN625 Multi-materials

The multi-material samples were fabricated by producing SS316L half blocks via LPBF using the same parameters and powder as the single alloy samples. The blocks were stress relieved and removed from the build plate through wire EDM and sent to the

⁴ Melt Pool Size Control (MPSC) is the in-situ closed-loop feedback cycle used by FormAlloy to change laser power based on the size of the melt pool detected by a camera.

DED manufacturer. IN625 was deposited onto the half blocks using DED with the same powder and parameters as the AM single alloy samples. One of the blocks had a direct transition with only IN625 powder deposited onto the LPBF SS316L half block, while the other half block had an intermediate zone that was two layers thick (600 μm total) of an in-situ mix of 50% SS316L powder and 50% IN625 powder. The full builds were stress relieved and detached from the build plate with wire EDM. The subsize ASTM E8 specimens were extracted via waterjet and then machined to thickness. The average cross-sectional area was 22.67 mm^2 with a standard deviation of 0.33 mm^2 , a minimum value of 22.21 mm^2 , and a maximum value of 23.29 mm^2 .

4.3 Results and Discussion

The stress-strain responses comparing the single alloy wrought and LPBF SS316L samples are recorded in Fig. 4.1. It is observed that the LPBF SS316L has higher YS (average value of 438 MPa), lower % El (average of 74 compared to 106), and a slightly lower UTS (average 626 MPa) compared to the wrought SS316L. The fractography images reveal ductile characteristics with localized plastic deformation.

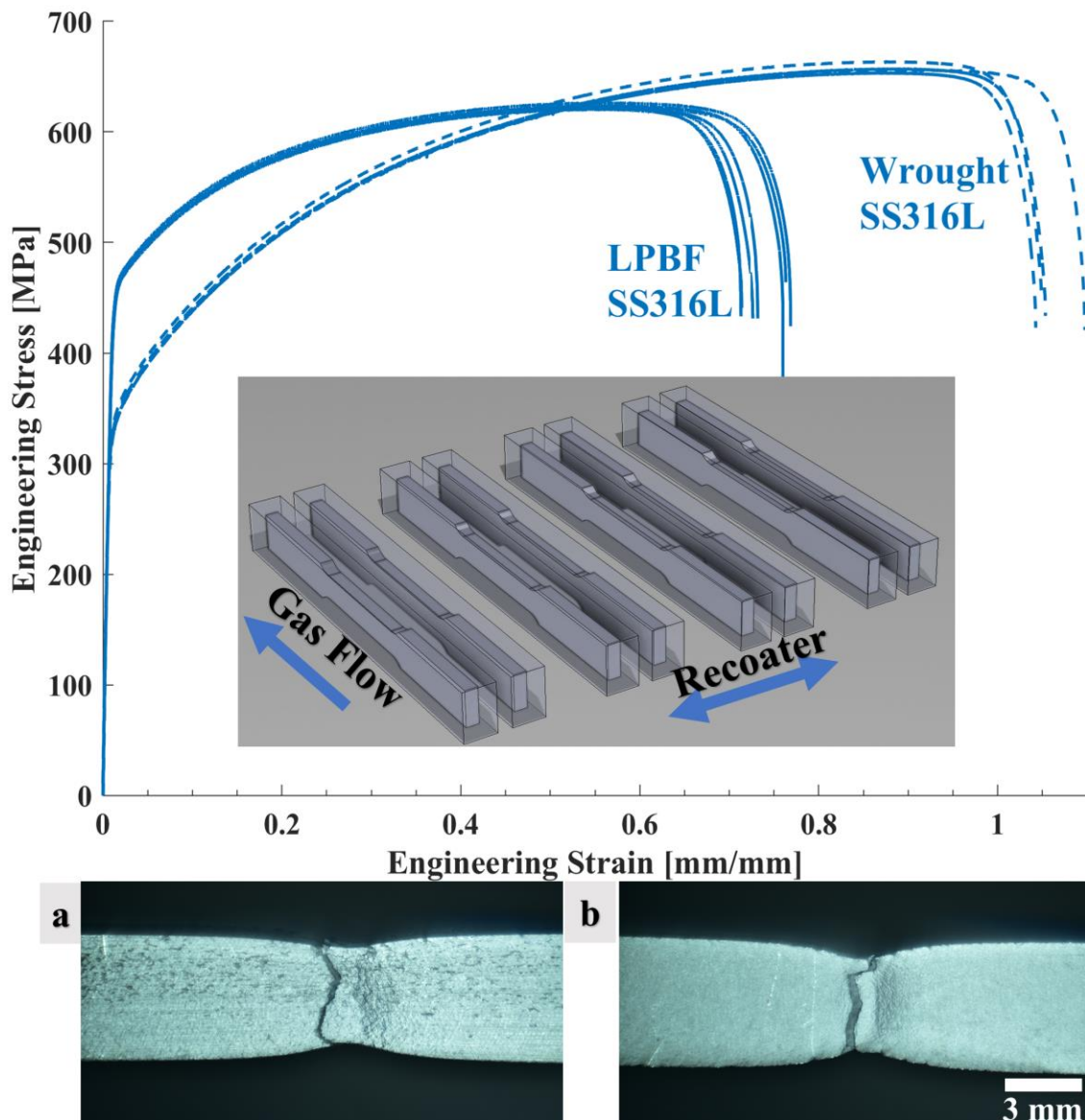


Fig. 4.1 Comparing engineering stress-strain curves of wrought SS316L to LPBF SS316L. The image of the build plate shows an YZ orientation. The fractography image (a) shows ductile failure of LPBF SS316L and (b) shows the wrought SS316L.

Fig. 4.2 demonstrates the tensile behaviors of single material wrought IN625 compared to DED IN625. The DED IN625 was extracted from a bulk material to ensure testing of anisotropic characteristics.

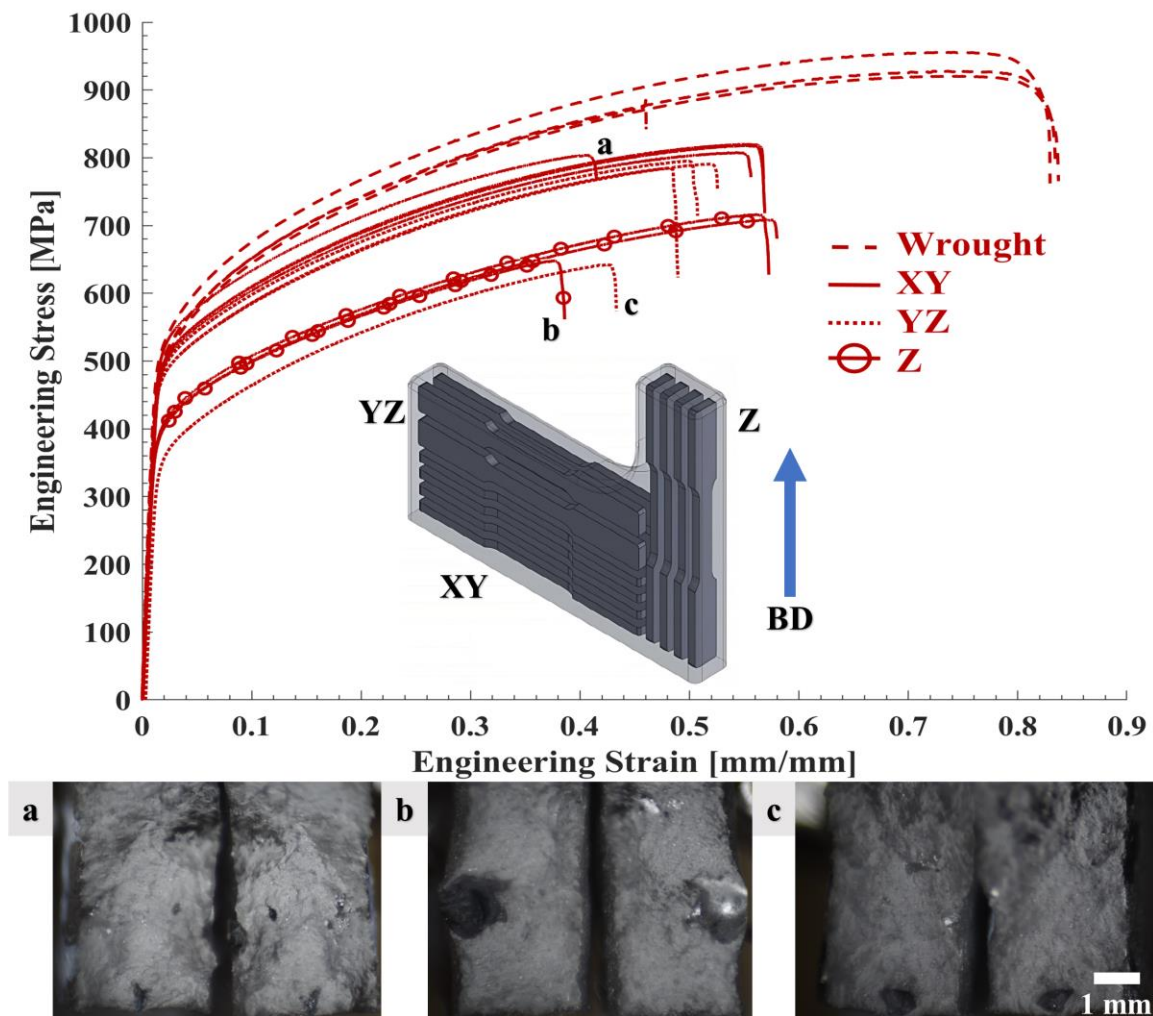


Fig. 4.2 Comparing engineering stress-strain curves of annealed wrought sheet coil IN625 to DED IN625 including directionality. Curves labeled a, b, and c correspond to the fractography images showing black particles.

Wrought IN625 has a higher elongation until fracture (average 74) that leads to increased toughness compared to the DED IN625. Anisotropy is demonstrated where the Z-oriented samples had lower YS and UTS (averages 367 and 707 MPa, respectively) compared to the XY-oriented samples (averages 433 and 780 MPa, respectively). Elongation to fracture was not affected by the print orientations (Averages of 57 and 56%). There were several notable samples that fractured at lower elongations than the rest of the samples and are denoted in Fig. 4.2 with the letters a, b, and c. Upon examination of the fracture surfaces, dark particles were observed. The particles were analyzed through EDS and the results can be seen in the inset of Fig. 4.3.

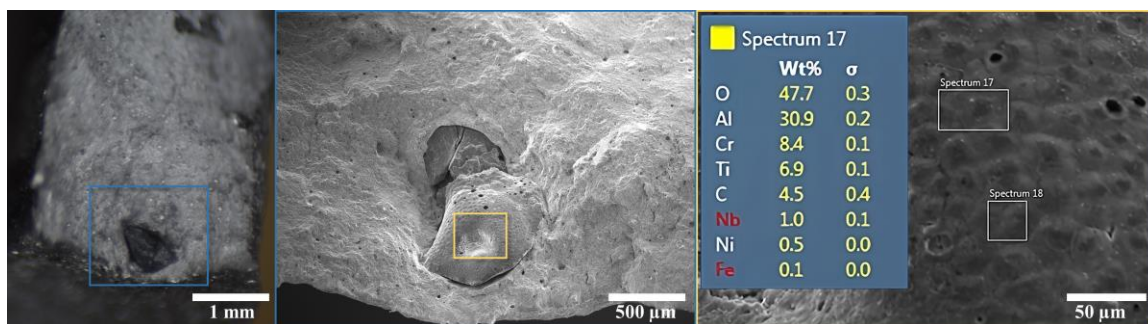


Fig. 4.3 Images of EDS analysis showing magnified images and chemical composition of particle found at the fracture surfaces of some IN625 samples fabricated by powder-fed DED.

The particles have the right chemical proportions of aluminum and oxygen to be considered aluminum oxide powder, also known as alumina, and are suspected to have contaminated the build from the powder feeding system during the transition of the system from a prior material system.

The tensile behavior of the multi-material samples, both direct transition and 50/50 intermediate transition, are shown in Fig. 4.4. Observations when comparing the tensile behavior of the multi-material samples include better elongation until fracture for the direct transition samples when compared to the 50/50 intermediate joint samples

(average of 37 versus 14). Striations are prominent in the fractography images for two of the samples that had a brittle fracture and are referred to as samples a and b in Figure Fig. 4.4. The authors hypothesize that the more brittle fracture is due to brittle carbides and Laves phases present in those samples [1].

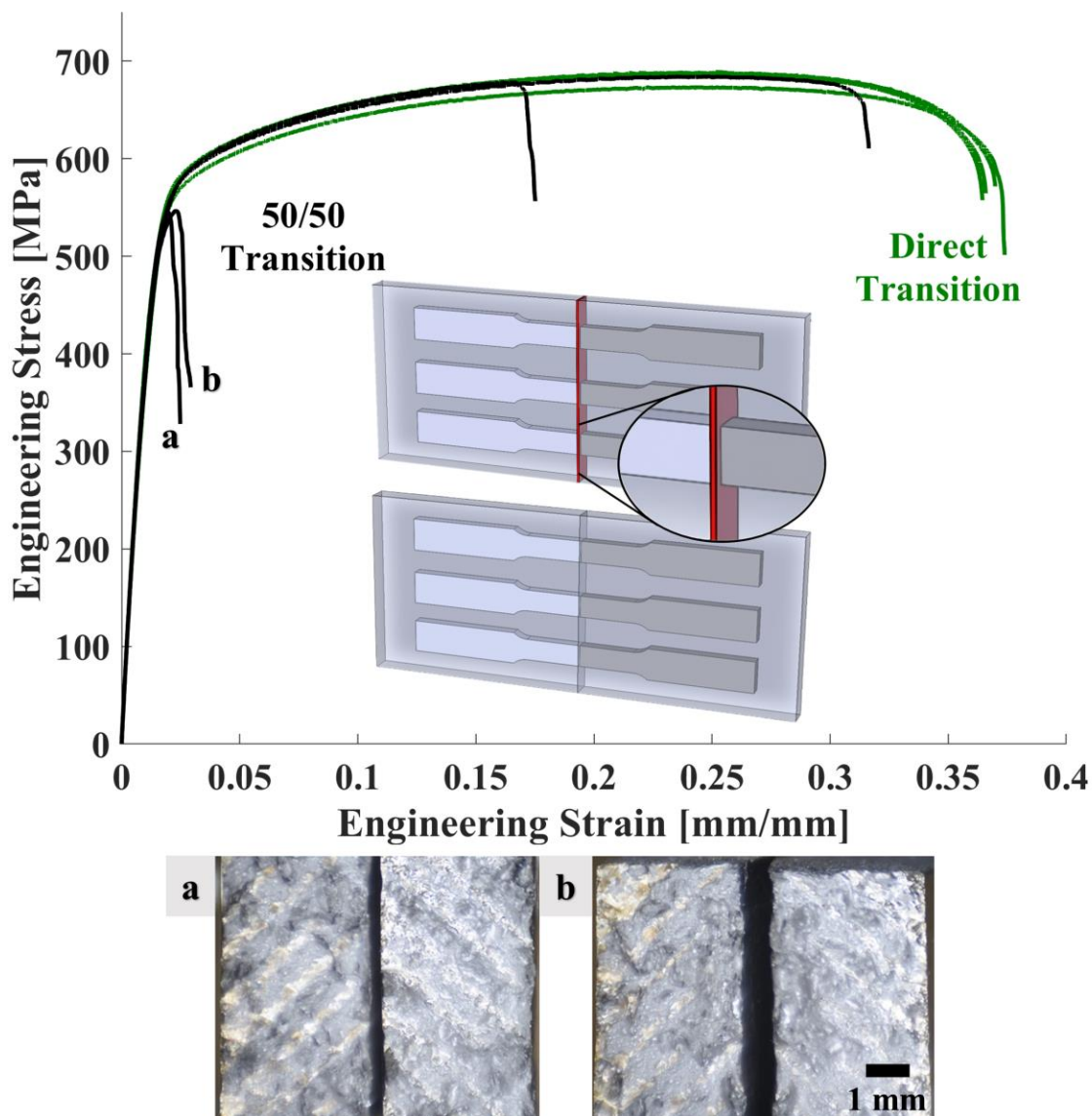


Fig. 4.4 Comparing engineering stress-strain curves of joining methods, namely, direct transition and 50/50 intermediate transition in DED IN625 deposited onto LPBF SS316L.

Curves labeled a and b correspond to the fractography images (a) and (b) showing striations at the fracture surfaces.

The tensile properties of the multi-material samples and single-alloy samples are illustrated in Fig. 4.5. Percent elongation until fracture was lower for both multi-materials compared to the single alloy AM and wrought samples. The UTS of the Direct Transition (average 684 MPa) samples exceeded that of the wrought SS316L (average 681 MPa) and approached that of IN625 printed in the Z orientation (average 707 MPa). Most remarkably, the YS of the multi-materials is higher than that of any of the single alloy counterparts. One explanation for this behavior could be that the manufacturer chose not to stress relieve the parts and residual thermal stresses remained. Warpage of the bulk material was observed after extracting the multi-material samples which provides further support that residual stresses were present in the material. Another explanation could be that the stress relief performed by the DED manufacturer was for IN625 which has a higher stress relief temperature. The industry recommended stress relief temperature of IN625 is 870°C [61]. This is well above the transformation temperature of ferrite–pearlite to austenite (A_{c1}), typically 730-790°C, that would then transform to pearlite upon cooling [62]. Garrison [63] has attributed the increase in the tensile strength of steel to an increase in pearlite.

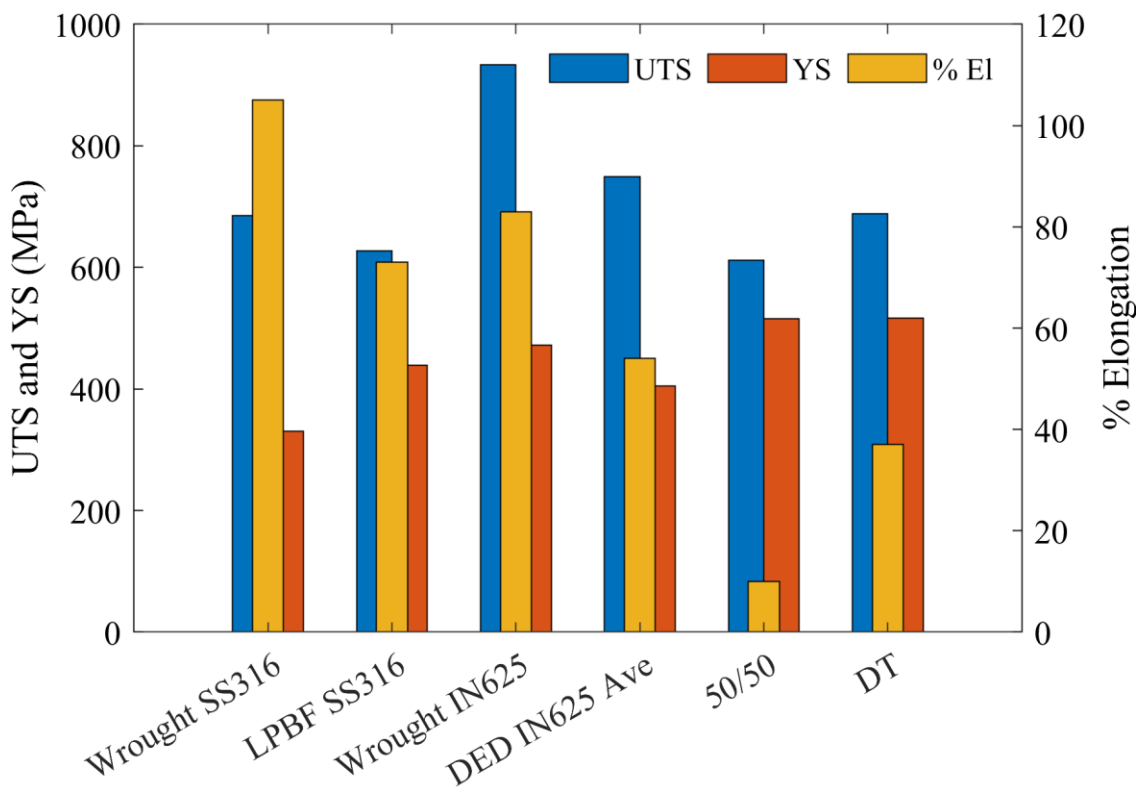


Fig. 4.5 Comparison of median values of the tensile properties of single-alloy samples and multi-materials.

Upon examining the samples post-mortem in Fig. 4.6, the 50/50 samples exhibited brittle fracture, while the direct transition samples were more ductile. The plastic deformation appears to have only affected the stainless steel regions of the samples with fracture occurring within the 50/50 intermediate region for the 50/50 samples, while fracture occurred within the stainless steel region of the direct transition samples. This was confirmed using an EDS line scan across the fractured specimens and results can be seen in Fig. 4.7.

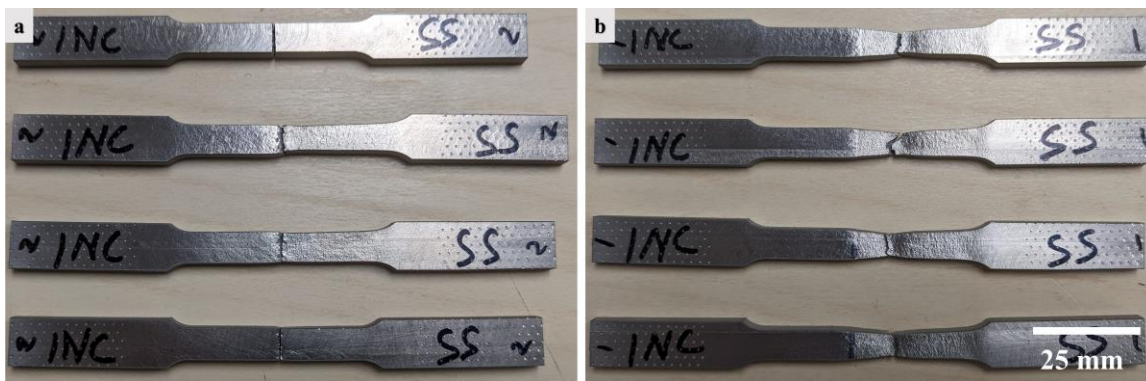


Fig. 4.6 Side-by-side comparison of post-mortem tensile dogbones a) 50/50 transition b) direct transition samples.

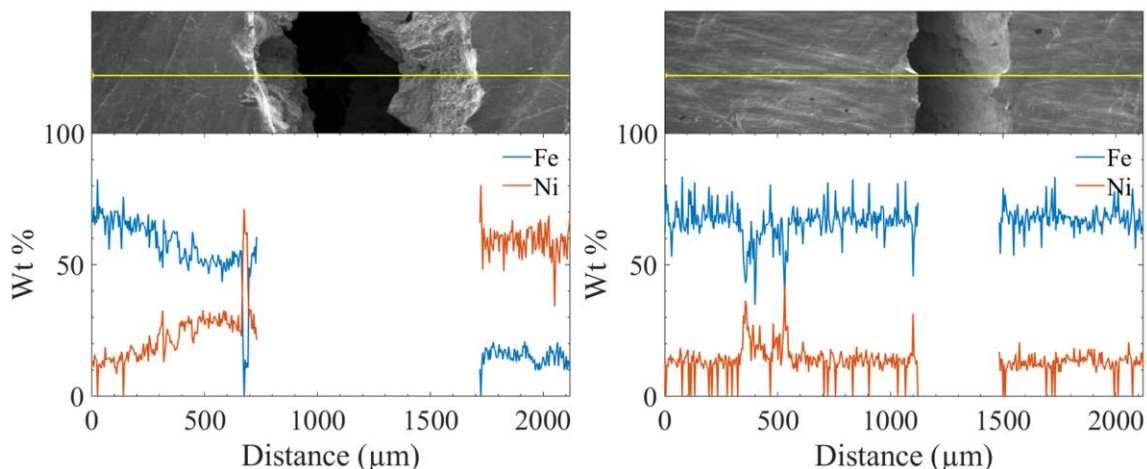


Fig. 4.7 EDS line scans across the fracture surface of a 50/50 transition sample (left) and a direct transition sample (right) where blue represents the Fe content and orange is the Ni.

Fig. 3.7 shows the EDS line scans across the two fracture sides of the multi-material samples. The Fe and Ni content can be seen closing the gap while moving from left to right in the 50/50 sample (Fig. 3.7 left). It then shows a transition to complete IN625 as the Ni content increases while the Fe content drops to a range of 10-20 wt%. In contrast, the fracture in the direct transition sample (Fig. 3.7 right) is evidently located on the SS316L side, as indicated by the constant levels of Fe and Ni throughout the scan.

Further analysis of the 50/50 transition region revealed microcracks at the transition from SS316L to the 50/50 intermediate zone. The authors postulate that the

microcracks present in the transition region drove the brittle failure as the cracks would introduce a crack-initiation site for propagation. Another crack was observed in the SS316L side approximately 500 μm from the transition (See Fig. 4.8).

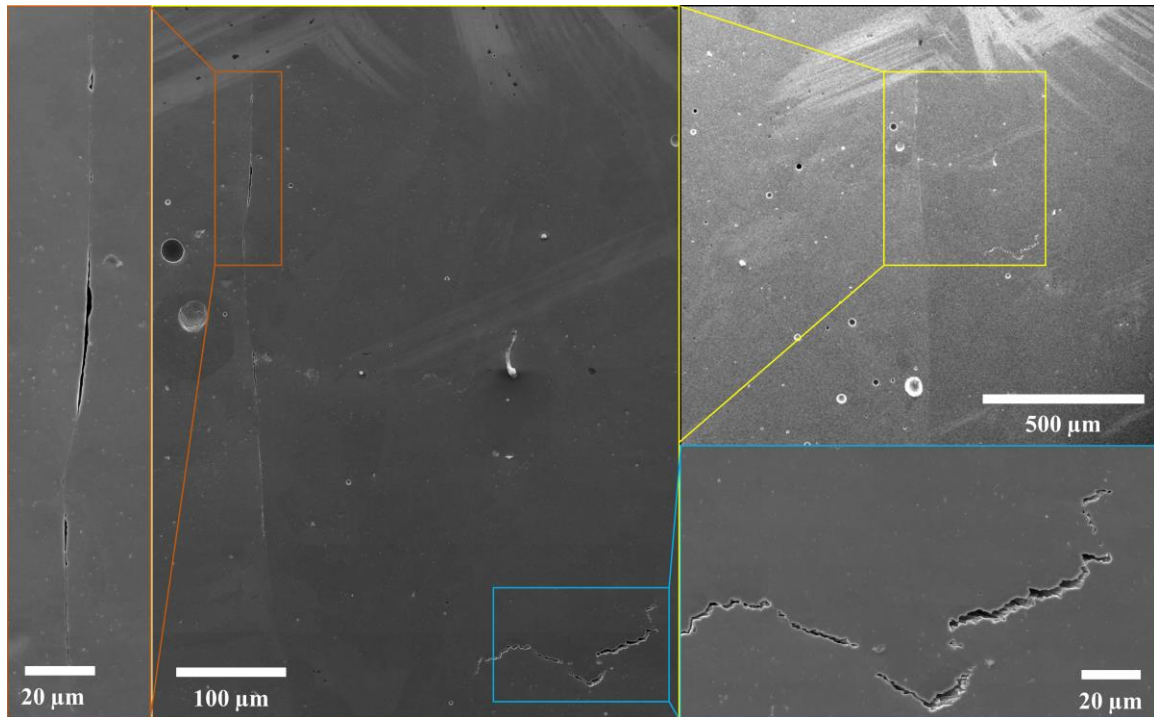


Fig. 4.8 SEM montage images of microcracks at the 50/50 transition in the multi-material samples.

The authors postulate that the cracking is due to the chosen processing parameters as processing parameter development was outside of the scope of the current project. Cracks develop in austenitic stainless steels during LPBF due to the presence of liquid films. The combination of these liquid films and thermal stresses resulting from LPBF leads to the formation of solidification cracks [64]. This means that both process parameters and the solidification sequence can influence cracking. Consequently, optimizing the chemical composition of the alloy can reduce the susceptibility of austenitic stainless steels to solidification cracking. In contrast to nickel superalloys, which are prone to various types of cracking like liquation and environmentally-assisted

cracking, solidification cracking is the sole type observed during LPBF of austenitic stainless steels.

Comparison of tensile values to literature is challenging as there has been no work on combining LPBF SS316L to IN625 via DED. However, others have used both techniques to combine similar alloys together with the same additive technique. Fig. 4.9 shows the comparison of median values of UTS, YS, and % El of the multi-materials in this work to that of similar research.

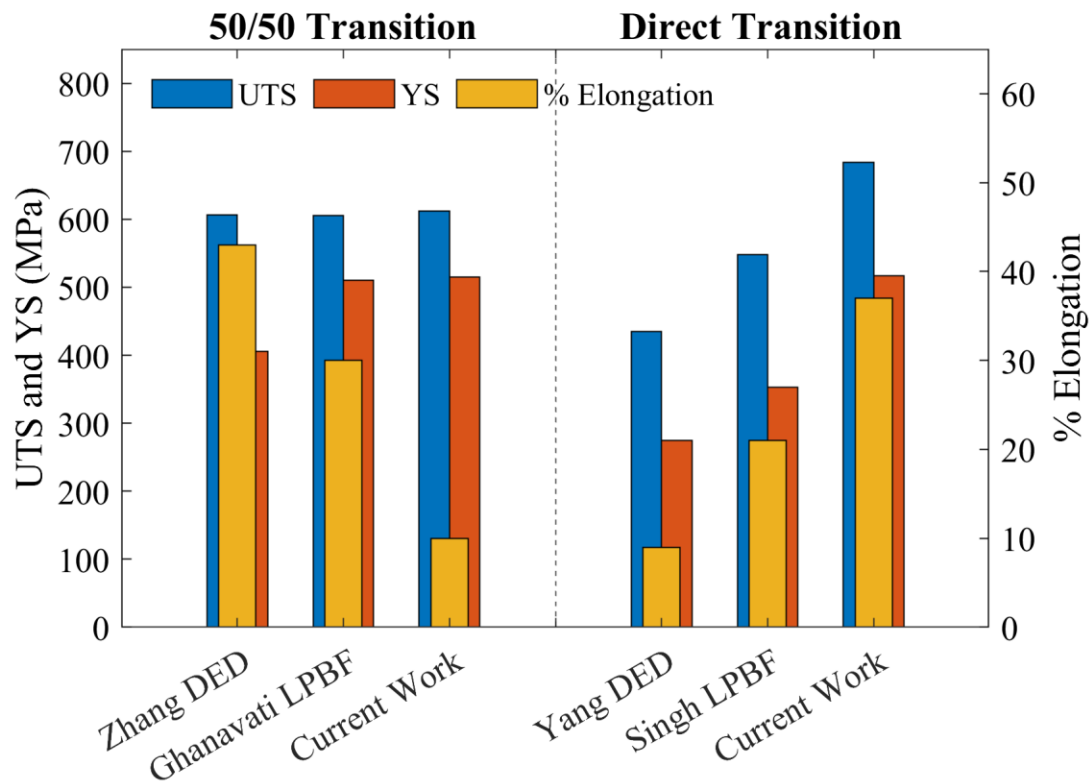


Fig. 4.9 Comparison of mechanical properties for average values from literature compared to median values of the current work. Zhang printed IN625 onto SS316L via DED with a 2 mm transition zone [11]. Ghanavati printed LPBF IN718 onto SS316L with a 4 mm transition zone [58]. Yang (DED) and Singh (LPBF) both used the print sequence of SS316L onto IN718 [18], [59].

The trend in tensile values compared to literature for the direct transition samples shows the current work outperformed the literature values substantially. This was likely

due to the fact that the current work deposited IN625 onto SS316L, whereas Yang et al. [59] and Singh et al. [18] both deposited SS316L onto IN718. Chen et al. [16] showed that printing sequence affects crack formation during fabrication of multi-materials made with DED IN625 and SS316L [16]. When SS316L was deposited onto IN625, it had a higher susceptibility to cracking than if the sequence were opposite and IN625 was deposited onto SS316L. Further work could prove that the increased tensile values is purely due to printing sequence, or if it is an unforeseen benefit of combining DED and LPBF. The trend in the 50/50 transition values between the literature values and the current work are nearly identical, however, elongation values appear much lower than that of the literature values. The results for the current work represent median value with the % El values for two of the four samples around 20 and 30% which is in closer agreement to literature values, however, the other two values were approximately 3% which significantly lowered the median value.

4.4 Conclusion

The novel combination of powder-fed DED with LPBF base material was successfully demonstrated. Multi-material LPBF-SS316L/DED-IN625 samples with a direct transition outperformed the intermediate 600 μm layer of 50% SS316L and 50% IN625 transition samples. Cracks were present in the 50/50 transition samples and were likely the cause for the brittle failure observed. Improvements to the processing parameters, or different mixing ratios could lead to a reduction in cracking.

Comparing the multi-material samples to single alloy counterparts, it is clear that the multi-material samples have an increased yield strength, less ductility, and UTS approaching that of DED-IN625. The higher yield strength is possibly due to higher

stress relief temperatures after fabrication of the DED material onto the LPBF SS316L, or a lack of any stress relief procedure resulting in higher residual stresses.

Within the single alloy DED-IN625 samples, aluminum oxide particles of varying sizes were present. This may be due to cross-contamination of powders in the powder feeding system of the DED machine from previous builds. This highlights the stringent needs in system cleanup when using DED fabrication techniques for multi-material components.

These findings emphasize the importance of optimizing multi-material bonding techniques in advanced manufacturing processes. Further research should be conducted to determine optimal mixing ratios for a more ductile and crack-free intermediate transition. Testing on a graded transition would also be insightful to compare its properties to the results from this work.

4.5 Declaration of Competing Interest

The authors declare that they have no known competing financial interests or personal relationships that could have appeared to influence the work reported in this paper.

4.6 Acknowledgements

This material is based upon work supported by the U.S. Department of Energy, Office of Science, Office of Energy and Renewable Energy, Solar Energy Technologies Office (SETO) under Award Number DE-EE0009381. The authors acknowledge startup funding from Utah State University. We acknowledge the support from the Microscopy Core Facility at Utah State University for the SEM result.

4.7 Data Availability

Data will be made available upon reasonable request to the corresponding author.

CHAPTER 5

DED H282 PRELIMINARY TEST

5.1 Introduction

One candidate material that was tested to be joined to the SS316L was H282. This material is a Nickel-based superalloy that is produced by Haynes International. The microstructure was analyzed as well as the tensile properties.

5.2 Methodology

The H282 alloy was produced through powder-fed DED. Microstructural analysis and tensile testing were performed in a similar manner discussed in the previous methodology sections from 3.2 and 4.2. The geometry of the samples is shown in Fig. 5.1 below. The average cross-sectional area of the samples was 21.17 mm^2 with a standard deviation of 0.665 mm . The range of values for area were between 20.20 mm to 22.15 mm . The samples had to be adjusted in thickness compared to the SS316L and IN625 samples to prevent the load from reaching the maximum range of the load cell of 25 kN .

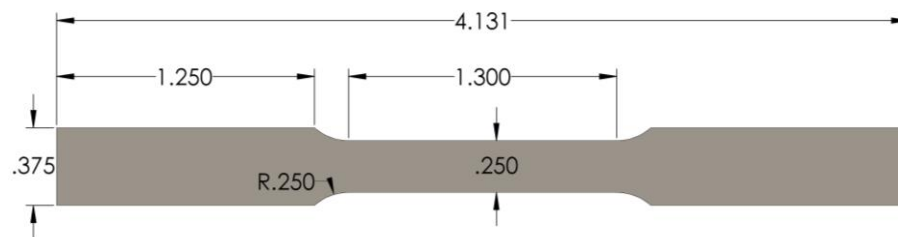


Fig. 5.1 Geometry of tensile samples.

5.3 Results and Discussion

The microstructural results from an EBSD analysis include an IPF-Z map, an histogram of grain diameter measured using the maximum Ferret diameter, and an inverse pole figure images. These results are shown in Fig. 5.2.

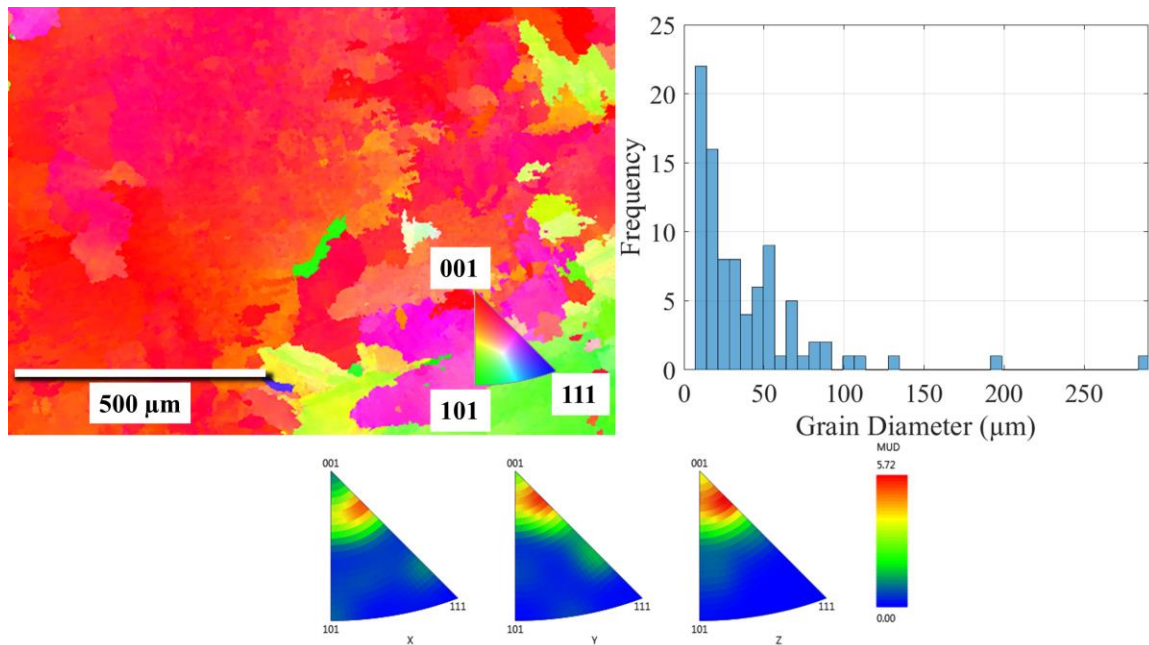


Fig. 5.2 Microstructural results of H282 manufactured by DED showing an IPF-Z map, a histogram of grain diameter, and inverse pole figures with x, y, and z from left to right.

It is observed that there exists a preferential orientation in the 001 direction. The MUD value is small in comparison to that of IN625 and would indicate a weaker preference. Increasing the sample size of regions characterized by EBSD would provide a more complete and representative dataset to be conclusive on grain orientation preference. Grain size appears to have the majority being less than 100 μm . The total number of grains was 89, further validating the need for more characterizations to get a larger sample size.

Tensile results were used to determine if the candidate material would be joined to SS316L. Three orientations were tested to determine any anisotropic properties. The results are shown in Fig. 5.3. Fractography images are presented of three samples that did not behave similarly to the rest of the samples.

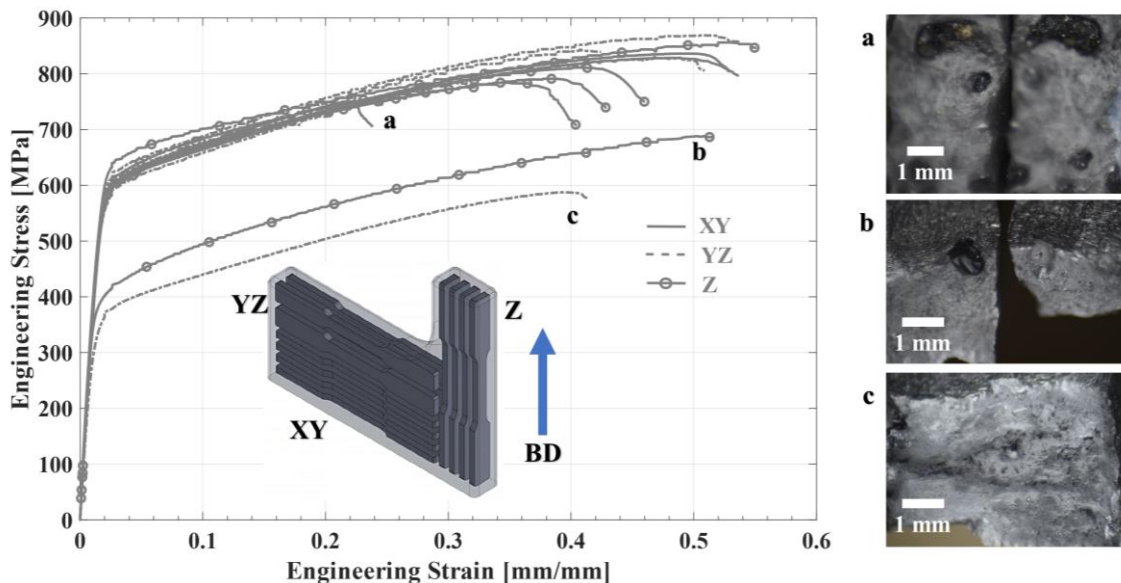


Fig. 5.3 Stress-strain curves for H282 manufactured through DED with samples tested in three different orientations (XY, YZ, and Z), fractography images from samples that differed in response when compared to the other samples (right).

The tensile results of the DED H282 were compared to the ASTM standard for wrought H282 values. The DED H282 did not meet the minimum required properties to be considered H282 and a heat treatment process would be required to enhance its properties. IN625 was thus chosen as the multi-material candidate due to its enhanced properties when printed compared to wrought IN625 ASTM values. The selection of IN625 eliminated the need for a heat treatment process and would further reduce time and cost.

CHAPTER 6

CONCLUSION

In conclusion, a comprehensive analysis of the microstructures of single alloy LPBF SS316L and DED IN625, as well as combinatory alloys featuring a direct transition and a 50/50 mixed intermediate region, was conducted. The study revealed elemental segregation during the deposition and solidification of the DED mixed layers, with microhardness measurements indicating higher hardness at the direct transition compared to the 50/50 transition.

The successful demonstration of the novel combination of powder-fed DED with LPBF base material was achieved. Multi-material samples with a direct transition exhibited superior performance over samples with an intermediate 600 μm layer of 50% SS316L and 50% IN625 transition. Cracks observed in the 50/50 transition samples were likely contributors to the observed brittle failure, suggesting that potential enhancements in processing parameters or adjustments to mixing ratios could mitigate cracking.

A comparison between the multi-material samples and their single alloy counterparts highlighted increased YS, reduced ductility, and UTS approaching that of DED-IN625. The elevated yield strength may be attributed to higher stress relief temperatures post-fabrication of DED material onto LPBF SS316L or the absence of a stress relief procedure, leading to heightened residual stresses.

In the case of single alloy DED-IN625 samples, the presence of aluminum oxide particles of varying sizes indicated possible cross-contamination of powders within the DED machine's powder feeding system from previous builds, underscoring a drawback of using DED for multi-material fabrication.

These findings emphasize the significance of optimizing multi-material bonding techniques in advanced manufacturing processes. Further research is warranted to identify optimal mixing ratios for achieving a more ductile and crack-free intermediate transition, and exploring testing on a graded transition would provide valuable insights for comparing its properties with the results obtained in this study. To help increase the application to heat exchangers, research in high temperature testing should be pursued.

REFERENCES

- [1] B. Aydogan, A. O'Neil, and H. Sahasrabudhe, "Microstructural and mechanical characterization of stainless steel 420 and Inconel 718 multi-material structures fabricated using laser directed energy deposition," *J. Manuf. Process.*, vol. 68, pp. 1224–1235, Aug. 2021, doi: 10.1016/j.jmapro.2021.06.031.
- [2] C. Wei, Z. Zhang, D. Cheng, Z. Sun, M. Zhu, and L. Li, "An overview of laser-based multiple metallic material additive manufacturing: from macro- to micro-scales," *Int. J. Extreme Manuf.*, vol. 3, no. 1, p. 012003, Dec. 2020, doi: 10.1088/2631-7990/abce04.
- [3] A. Nazir *et al.*, "Multi-material additive manufacturing: A systematic review of design, properties, applications, challenges, and 3D printing of materials and cellular metamaterials," *Mater. Des.*, vol. 226, p. 111661, Feb. 2023, doi: 10.1016/j.matdes.2023.111661.
- [4] M. Vaezi, S. Chianrabutra, B. Mellor, and S. Yang, "Multiple material additive manufacturing – Part 1: a review: This review paper covers a decade of research on multiple material additive manufacturing technologies which can produce complex geometry parts with different materials," *Virtual Phys. Prototyp.*, vol. 8, no. 1, pp. 19–50, Mar. 2013, doi: 10.1080/17452759.2013.778175.
- [5] Y. Su, B. Chen, C. Tan, X. Song, and J. Feng, "Influence of composition gradient variation on the microstructure and mechanical properties of 316 L/Inconel718 functionally graded material fabricated by laser additive manufacturing," *J. Mater. Process. Technol.*, vol. 283, p. 116702, Sep. 2020, doi: 10.1016/j.jmatprotec.2020.116702.
- [6] D. R. Feenstra, R. Banerjee, H. L. Fraser, A. Huang, A. Molotnikov, and N. Birbilis, "Critical review of the state of the art in multi-material fabrication via directed energy deposition," *Curr. Opin. Solid State Mater. Sci.*, vol. 25, no. 4, p. 100924, Aug. 2021, doi: 10.1016/j.cossms.2021.100924.
- [7] C. Tan *et al.*, "Ultra-strong bond interface in additively manufactured iron-based multi-materials," *Mater. Sci. Eng. -Struct. Mater. Prop. Microstruct. Process.*, vol. 802, p. 140642, 2021, doi: 10.1016/j.msea.2020.140642.
- [8] D. T. Sarathchandra, S. Kanmani Subbu, and N. Venkaiah, "Functionally graded materials and processing techniques: An art of review," *Mater. Today Proc.*, vol. 5, no. 10, Part 1, pp. 21328–21334, Jan. 2018, doi: 10.1016/j.matpr.2018.06.536.
- [9] S. Hasanov *et al.*, "Review on Additive Manufacturing of Multi-Material Parts: Progress and Challenges," *J. Manuf. Mater. Process.*, vol. 6, no. 1, Art. no. 1, Feb. 2022, doi: 10.3390/jmmp6010004.

- [10] X. Lin, T. M. Yue, H. O. Yang, and W. D. Huang, "Laser rapid forming of SS316L/Rene88DT graded material," *Mater. Sci. Eng. A*, vol. 391, no. 1, pp. 325–336, Jan. 2005, doi: 10.1016/j.msea.2004.08.072.
- [11] X. Zhang, Y. Chen, and F. Liou, "Fabrication of SS316L-IN625 functionally graded materials by powder-fed directed energy deposition," *Sci. Technol. Weld. Join.*, vol. 24, no. 5, pp. 504–516, Jul. 2019, doi: 10.1080/13621718.2019.1589086.
- [12] S. Mohd Yusuf, X. Zhao, S. Yang, and N. Gao, "Interfacial characterisation of multi-material 316L stainless steel/Inconel 718 fabricated by laser powder bed fusion," *Mater. Lett.*, vol. 284, p. 128928, Feb. 2021, doi: 10.1016/j.matlet.2020.128928.
- [13] A. Hinojos *et al.*, "Joining of Inconel 718 and 316 Stainless Steel using electron beam melting additive manufacturing technology," *Mater. Des.*, vol. 94, pp. 17–27, Mar. 2016, doi: 10.1016/j.matdes.2016.01.041.
- [14] W.-Y. Chen, X. Zhang, M. Li, R. Xu, C. Zhao, and T. Sun, "Laser powder bed fusion of Inconel 718 on 316 stainless steel," *Addit. Manuf.*, vol. 36, p. 101500, Dec. 2020, doi: 10.1016/j.addma.2020.101500.
- [15] D. Wu, X. Liang, Q. Li, and L. Jiang, "Laser Rapid Manufacturing of Stainless Steel 316L/Inconel718 Functionally Graded Materials: Microstructure Evolution and Mechanical Properties," *Int. J. Opt.*, vol. 2010, p. e802385, Jan. 2011, doi: 10.1155/2010/802385.
- [16] N. Chen *et al.*, "Microstructural characteristics and crack formation in additively manufactured bimetal material of 316L stainless steel and Inconel 625," *Addit. Manuf.*, vol. 32, p. 101037, Mar. 2020, doi: 10.1016/j.addma.2020.101037.
- [17] K. Shah, I. ul Haq, A. Khan, S. A. Shah, M. Khan, and A. J. Pinkerton, "Parametric study of development of Inconel-steel functionally graded materials by laser direct metal deposition," *Mater. Des. 1980-2015*, vol. 54, pp. 531–538, Feb. 2014, doi: 10.1016/j.matdes.2013.08.079.
- [18] S. P. Singh, A. Aggarwal, R. K. Upadhyay, and A. Kumar, "Processing of IN718-SS316L bimetallic-structure using laser powder bed fusion technique," *Mater. Manuf. Process.*, vol. 36, no. 9, pp. 1028–1039, Jul. 2021, doi: 10.1080/10426914.2021.1885701.
- [19] J. Kerry, "The Long-Term Strategy of the United States, Pathways to Net-Zero Greenhouse Gas Emissions by 2050".
- [20] "U.S. energy facts explained - consumption and production - U.S. Energy Information Administration (EIA)." Accessed: Apr. 19, 2023. [Online]. Available:

<https://www.eia.gov/energyexplained/us-energy-facts/>

- [21] H. L. Zhang, J. Baeyens, J. Degève, and G. Cacères, “Concentrated solar power plants: Review and design methodology,” *Renew. Sustain. Energy Rev.*, vol. 22, pp. 466–481, Jun. 2013, doi: 10.1016/j.rser.2013.01.032.
- [22] D. Barlev, R. Vidu, and P. Stroeve, “Innovation in concentrated solar power,” *Sol. Energy Mater. Sol. Cells*, vol. 95, no. 10, pp. 2703–2725, Oct. 2011, doi: 10.1016/j.solmat.2011.05.020.
- [23] C. F. McDonald, “Low Cost Recuperator Concept for Microturbine Applications,” presented at the ASME Turbo Expo 2000: Power for Land, Sea, and Air, American Society of Mechanical Engineers Digital Collection, Aug. 2014. doi: 10.1115/2000-GT-0167.
- [24] C. F. McDonald, “Recuperator considerations for future higher efficiency microturbines,” *Appl. Therm. Eng.*, vol. 23, no. 12, pp. 1463–1487, Aug. 2003, doi: 10.1016/S1359-4311(03)00083-8.
- [25] B. Saleh *et al.*, “30 Years of functionally graded materials: An overview of manufacturing methods, Applications and Future Challenges,” *Compos. Part B Eng.*, vol. 201, p. 108376, Nov. 2020, doi: 10.1016/j.compositesb.2020.108376.
- [26] D. Dev Singh, S. Arjula, and A. Raji Reddy, “Functionally Graded Materials Manufactured by Direct Energy Deposition: A review,” *Mater. Today Proc.*, vol. 47, pp. 2450–2456, 2021, doi: 10.1016/j.matpr.2021.04.536.
- [27] M. Schneck, M. Horn, M. Schmitt, C. Seidel, G. Schlick, and G. Reinhart, “Review on additive hybrid- and multi-material-manufacturing of metals by powder bed fusion: state of technology and development potential,” *Prog. Addit. Manuf.*, vol. 6, no. 4, pp. 881–894, Dec. 2021, doi: 10.1007/s40964-021-00205-2.
- [28] E. Rasouli *et al.*, “Design and Performance Characterization of an Additively Manufactured Primary Heat Exchanger for sCO₂ Waste Heat Recovery Cycles”.
- [29] R. Tiwari, R. S. Andhare, A. Shooshtari, and M. Ohadi, “Development of an additive manufacturing-enabled compact manifold microchannel heat exchanger,” *Appl. Therm. Eng.*, vol. 147, pp. 781–788, Jan. 2019, doi: 10.1016/j.applthermaleng.2018.10.122.
- [30] M. Ding *et al.*, “An adaptive flow path regenerator used in supercritical carbon dioxide Brayton cycle,” *Appl. Therm. Eng.*, vol. 138, pp. 513–522, Jun. 2018, doi: 10.1016/j.applthermaleng.2018.04.055.
- [31] I. Kaur and P. Singh, “State-of-the-art in heat exchanger additive manufacturing,” *Int. J. Heat Mass Transf.*, vol. 178, p. 121600, Oct. 2021, doi: 10.1016/j.ijheatmasstransfer.2021.121600.

- [32] W. W. Wits and E. Amsterdam, "Graded structures by multi-material mixing in laser powder bed fusion," *CIRP Ann.*, vol. 70, no. 1, pp. 159–162, Jan. 2021, doi: 10.1016/j.cirp.2021.03.005.
- [33] A. Mussatto, "Research progress in multi-material laser-powder bed fusion additive manufacturing: A review of the state-of-the-art techniques for depositing multiple powders with spatial selectivity in a single layer," *Results Eng.*, vol. 16, p. 100769, Dec. 2022, doi: 10.1016/j.rineng.2022.100769.
- [34] S. Ali *et al.*, "Microstructure and Mechanical Properties of Modified 316L Stainless Steel Alloy for Biomedical Applications Using Powder Metallurgy," *Materials*, vol. 15, no. 8, Art. no. 8, Jan. 2022, doi: 10.3390/ma15082822.
- [35] C. Zhong, J. Kittel, A. Gasser, and J. H. Schleifenbaum, "Study of nickel-based super-alloys Inconel 718 and Inconel 625 in high-deposition-rate laser metal deposition," *Opt. Laser Technol.*, vol. 109, pp. 352–360, Jan. 2019, doi: 10.1016/j.optlastec.2018.08.003.
- [36] X. Wang, J. A. Muñiz-Lerma, M. Attarian Shandiz, O. Sanchez-Mata, and M. Brochu, "Crystallographic-orientation-dependent tensile behaviours of stainless steel 316L fabricated by laser powder bed fusion," *Mater. Sci. Eng. A*, vol. 766, p. 138395, Oct. 2019, doi: 10.1016/j.msea.2019.138395.
- [37] H. Sohrabpoor *et al.*, "Microstructural and mechanical evaluation of post-processed SS 316L manufactured by laser-based powder bed fusion," *J. Mater. Res. Technol.*, vol. 12, pp. 210–220, May 2021, doi: 10.1016/j.jmrt.2021.02.090.
- [38] M. R. Jandaghi, A. Saboori, L. Iuliano, and M. Pavese, "On the effect of rapid annealing on the microstructure and mechanical behavior of additively manufactured stainless steel by Laser Powder Bed Fusion," *Mater. Sci. Eng. A*, vol. 828, p. 142109, Nov. 2021, doi: 10.1016/j.msea.2021.142109.
- [39] S. Pratheesh Kumar, S. Elangovan, R. Mohanraj, and J. R. Ramakrishna, "A review on properties of Inconel 625 and Inconel 718 fabricated using direct energy deposition," *Mater. Today Proc.*, vol. 46, pp. 7892–7906, Jan. 2021, doi: 10.1016/j.matpr.2021.02.566.
- [40] N. Martin, A. Hor, E. Copin, P. Lours, and L. Ratsifandrihana, "Correlation between microstructure heterogeneity and multi-scale mechanical behavior of hybrid LPBF-DED Inconel 625," *J. Mater. Process. Technol.*, vol. 303, p. 117542, May 2022, doi: 10.1016/j.jmatprotec.2022.117542.
- [41] Y. Hu *et al.*, "Influence of heat treatments on the microstructure and mechanical properties of Inconel 625 fabricated by directed energy deposition," *Mater. Sci. Eng. A*, vol. 817, p. 141309, Jun. 2021, doi: 10.1016/j.msea.2021.141309.

- [42] F. Chen, Q. Wang, C. Zhang, Z. Huang, M. Jia, and Q. Shen, "Microstructures and mechanical behaviors of additive manufactured Inconel 625 alloys via selective laser melting and laser engineered net shaping," *J. Alloys Compd.*, vol. 917, p. 165572, Oct. 2022, doi: 10.1016/j.jallcom.2022.165572.
- [43] Y. Kong and H. Huang, "Effect of intrinsic heat treatment on microstructure and hardness of additively manufactured Inconel 625 alloy by directed energy deposition," *Mater. Des.*, vol. 224, p. 111279, Dec. 2022, doi: 10.1016/j.matdes.2022.111279.
- [44] J. Wang, Y. Wang, Y. Su, and J. Shi, "Evaluation of in-situ alloyed Inconel 625 from elemental powders by laser directed energy deposition," *Mater. Sci. Eng. A*, vol. 830, p. 142296, Jan. 2022, doi: 10.1016/j.msea.2021.142296.
- [45] A. Gamon *et al.*, "Microstructure and hardness comparison of as-built inconel 625 alloy following various additive manufacturing processes," *Results Mater.*, vol. 12, p. 100239, Dec. 2021, doi: 10.1016/j.rinma.2021.100239.
- [46] K. Benarji, Y. Ravi Kumar, A. N. Jinoop, C. P. Paul, and K. S. Bindra, "Effect of Heat-Treatment on the Microstructure, Mechanical Properties and Corrosion Behaviour of SS 316 Structures Built by Laser Directed Energy Deposition Based Additive Manufacturing," *Met. Mater. Int.*, vol. 27, no. 3, pp. 488–499, Mar. 2021, doi: 10.1007/s12540-020-00838-y.
- [47] Y. Wen *et al.*, "Microstructure-property correlations in as-built and heat-treated compositionally graded stainless steel 316L-Inconel 718 alloy fabricated by laser powder bed fusion," *Mater. Sci. Eng. A*, vol. 862, p. 144515, Jan. 2023, doi: 10.1016/j.msea.2022.144515.
- [48] S. H. Jagdale, S. Theeda, B. B. Ravichander, and G. Kumar, "Surface Morphology and Hardness of Powder Bed Fused Ss316l as a Function of Process Parameters," 2022. doi: 10.26153/tsw/44546.
- [49] D. Gu and H. Chen, "Selective laser melting of high strength and toughness stainless steel parts: The roles of laser hatch style and part placement strategy," *Mater. Sci. Eng. A*, vol. 725, pp. 419–427, May 2018, doi: 10.1016/j.msea.2018.04.046.
- [50] N. P. Lavery *et al.*, "Effects of hot isostatic pressing on the elastic modulus and tensile properties of 316L parts made by powder bed laser fusion," *Mater. Sci. Eng. A*, vol. 693, pp. 186–213, May 2017, doi: 10.1016/j.msea.2017.03.100.
- [51] M. Karmuhilan and S. Kumanan, "A Review on Additive Manufacturing Processes of Inconel 625," *J. Mater. Eng. Perform.*, vol. 31, no. 4, pp. 2583–2592, Apr. 2022, doi: 10.1007/s11665-021-06427-3.
- [52] T. Pan *et al.*, "Characteristics of Inconel 625—copper bimetallic structure

- fabricated by directed energy deposition," *Int. J. Adv. Manuf. Technol.*, vol. 109, no. 5, pp. 1261–1274, Jul. 2020, doi: 10.1007/s00170-020-05713-z.
- [53] T. C. Chawla, D. L. Graff, R. C. Borg, G. L. Bordner, D. P. Weber, and D. Miller, "Thermophysical properties of mixed oxide fuel and stainless steel type 316 for use in transition phase analysis," *Nucl. Eng. Des.*, vol. 67, no. 1, pp. 57–74, Oct. 1981, doi: 10.1016/0029-5493(81)90155-2.
- [54] R. Darabi, A. Ferreira, E. Azinpour, J. C. de Sa, and A. Reis, "Thermal study of a cladding layer of Inconel 625 in Directed Energy Deposition (DED) process using a phase-field model," *Int. J. Adv. Manuf. Technol.*, vol. 119, no. 5, pp. 3975–3993, Mar. 2022, doi: 10.1007/s00170-021-08376-6.
- [55] S. Mirzababaei *et al.*, "Remarkable enhancement in thermal conductivity of stainless-steel leveraging metal composite via laser powder bed fusion: 316L-Cu composite," *Addit. Manuf.*, vol. 70, p. 103576, May 2023, doi: 10.1016/j.addma.2023.103576.
- [56] J. C. Simmons *et al.*, "Influence of processing and microstructure on the local and bulk thermal conductivity of selective laser melted 316L stainless steel," *Addit. Manuf.*, vol. 32, p. 100996, Mar. 2020, doi: 10.1016/j.addma.2019.100996.
- [57] K. Halmešová, Z. Trojanová, M. Koukolíková, M. Brázda, J. Džugan, and W. Huang, "Effect of laser power on thermal properties of multimaterial structure Inconel 718 and stainless steel 316L processed by directed energy deposition," *J. Alloys Compd.*, vol. 927, p. 167082, Dec. 2022, doi: 10.1016/j.jallcom.2022.167082.
- [58] R. Ghanavati, E. Lannunziata, E. Norouzi, S. Bagherifard, L. Iuliano, and A. Saboori, "Design and development of SS316L-IN718 functionally graded materials via laser powder bed fusion," *Mater. Lett.*, vol. 349, p. 134793, Oct. 2023, doi: 10.1016/j.matlet.2023.134793.
- [59] S. W. Yang, J. Yoon, H. Lee, and D. S. Shim, "Defect of functionally graded material of inconel 718 and STS 316L fabricated by directed energy deposition and its effect on mechanical properties," *J. Mater. Res. Technol.*, vol. 17, pp. 478–497, Mar. 2022, doi: 10.1016/j.jmrt.2022.01.029.
- [60] C. J. Bettencourt and N. Kouraytem, "Microstructural Characterization of the Transition in SS316L and IN625 Bimetallic Fabricated Using Hybrid Additive Manufacturing," *JOM*, Oct. 2023, doi: 10.1007/s11837-023-06119-4.
- [61] A. Banerjee *et al.*, "Effect of stress-relief heat treatments on the microstructure and mechanical response of additively manufactured IN625 thin-walled elements," *Mater. Sci. Eng. A*, vol. 846, p. 143288, Jun. 2022, doi: 10.1016/j.msea.2022.143288.

- [62] K. D. Clarke, "12.10 - Austenite Formation and Microstructural Control in Low-Alloy Steels," in *Comprehensive Materials Processing*, S. Hashmi, G. F. Batalha, C. J. Van Tyne, and B. Yilbas, Eds., Oxford: Elsevier, 2014, pp. 345–361. doi: 10.1016/B978-0-08-096532-1.01211-5.
- [63] W. M. Garrison, "Steels: Classifications," in *Encyclopedia of Materials: Science and Technology*, K. H. J. Buschow, R. W. Cahn, M. C. Flemings, B. Ilshner, E. J. Kramer, S. Mahajan, and P. Veyssi re, Eds., Oxford: Elsevier, 2001, pp. 8840–8843. doi: 10.1016/B0-08-043152-6/01587-4.
- [64] H. E. Sabzi, S. Maeng, X. Liang, M. Simonelli, N. T. Aboulkhair, and P. E. J. Rivera-D az-del-Castillo, "Controlling crack formation and porosity in laser powder bed fusion: Alloy design and process optimisation," *Addit. Manuf.*, vol. 34, p. 101360, Aug. 2020, doi: 10.1016/j.addma.2020.101360.